


REPORT

Cdc42 GTPase regulates ESCRTs in nuclear envelope sealing and ER remodeling

Michelle Seiko Lu and David G. Drubin 

Small GTPases of the Rho family are binary molecular switches that regulate a variety of processes including cell migration and oriented cell divisions. Known Cdc42 effectors include proteins involved in cytoskeletal remodeling and kinase-dependent transcription induction, but none are involved in the maintenance of nuclear envelope integrity or ER morphology. Maintenance of nuclear envelope integrity requires the EndoSomal Complexes Required for Transport (ESCRT) proteins, but how they are regulated in this process remains unknown. Here, we show by live-cell imaging a novel Cdc42 localization with ESCRT proteins at sites of nuclear envelope and ER fission and, by genetic analysis of *cdc42* mutant yeast, uncover a unique Cdc42 function in regulation of ESCRT proteins at the nuclear envelope and sites of ER tubule fission. Our findings implicate Cdc42 in nuclear envelope sealing and ER remodeling, where it regulates ESCRT disassembly to maintain nuclear envelope integrity and proper ER architecture.

Introduction

Maintenance of the nuclear envelope is critical for compartmentalization of the activities of the nucleus away from those of the cytoplasm and requires the proper function of several proteins, including the ESCRT and LEM-family proteins (Gu et al., 2017; Lee et al., 2020; Olmos et al., 2016, 2015; Penfield et al., 2020; Thaller et al., 2019; Vietri et al., 2015; Webster et al., 2014, 2016). The ESCRTs are a family of membrane-deforming proteins that mediate reverse-topology scission of membranes (Schöneberg et al., 2017). Together with the inner nuclear membrane-embedded LEM-family proteins, the ESCRTs carry out the closure of holes (annular fusion) in the nuclear envelope (Olmos et al., 2016; Penfield et al., 2020). Loss of proper ESCRT and LEM protein function in open-mitosis systems results in the failure of postmitotic nuclear envelope reassembly, ultimately leading to delayed microtubule assembly, compromised nuclear integrity, and DNA damage (Olmos et al., 2015, 2016; Vietri et al., 2015; Penfield et al., 2020). In closed-mitosis systems such as those of *Saccharomyces cerevisiae* and *Schizosaccharomyces pombe*, wherein the nuclear envelope does not break down and instead undergoes fission, as well as the partially closed-mitosis system of *Schizosaccharomyces japonicus*, which undergoes partial NE breakdown and reassembly, ESCRT and LEM dysfunction results in the loss of nucleo-cytoplasmic partitioning (Gu et al., 2017; Lee et al., 2020; Thaller et al., 2019; Webster et al., 2014, 2016).

Proper ESCRT function relies on its ordered recruitment and assembly into organized filaments at membrane holes and areas

of high membrane curvature (Schöneberg et al., 2017). The dysregulation of its assembly can result in toxic nuclear envelope malformations, such as those seen in fission yeast over-expressing Lem2p, an inner nuclear membrane LEM-family protein that recruits the ESCRT-III component Cmp7p in fission yeast (Gonzalez et al., 2012; Gu et al., 2017; King et al., 2006). ESCRT-III disassembly must also be tightly regulated, as unrestricted ESCRT-III function can lead to large gaps in the nuclear envelope, as seen in fission yeast lacking Vps4, a type 1 AAA⁺ ATPase whose main cellular function appears to be to disassemble ESCRT filaments (Gu et al., 2017). Thus, both assembly and disassembly of ESCRTs must be carefully controlled in vivo to ensure nuclear envelope integrity.

While it is known that the ESCRT-III proteins, LEM-family proteins, and VPS4 are required for nuclear envelope sealing in mammalian cells, nematodes, fission yeast (*S. pombe* and *S. japonicus*), and budding yeast, how these components are regulated during this process is not yet clear. Here, we report our serendipitous discovery of a novel Cdc42-ESCRT-nuclear envelope connection through live-cell imaging approaches, which, combined with biochemical and genetic analyses of a *cdc42* mutant, reveal that the Rho family GTPase Cdc42 functions in regulation of ESCRT-III during nuclear envelope sealing and ER remodeling in budding yeast, either through direct regulation of ESCRT-III or indirectly through regulation of actin reorganization. Our data suggest that Cdc42 is a regulator of ESCRT-III

Department of Molecular and Cell Biology, University of California, Berkeley, Berkeley, CA.

Correspondence to David G. Drubin: drubin@berkeley.edu.

© 2020 Lu and Drubin. This article is distributed under the terms of an Attribution–Noncommercial–Share Alike–No Mirror Sites license for the first six months after the publication date (see <http://www.rupress.org/terms/>). After six months it is available under a Creative Commons License (Attribution–Noncommercial–Share Alike 4.0 International license, as described at <https://creativecommons.org/licenses/by-nc-sa/4.0/>).

filament disassembly through a Vps4-mediated mechanism at sites of annular fusion on the nuclear envelope and also to sites of ER tubule fission. This function represents a novel role for Cdc42, a molecular switch with well-known functions in actin polymerization (Kim et al., 2000; Prehoda et al., 2000), spindle positioning (Garrard et al., 2003; Gotta et al., 2001; Kay and Hunter, 2001), and exocytosis (Adamo et al., 2001; Zhang et al., 2001).

Results and discussion

Functional Cdc42 has never been imaged in live budding yeast cells because it is not amenable to N- or C-terminal protein fusions. In an effort to visualize Cdc42 in living cells, we created a functional Cdc42-mCherry internal fusion protein (Cdc42-mCherry^{sw}) in budding yeast analogous to that engineered previously in fission yeast (Bendezú et al., 2015). Unlike N-terminally tagged alleles of *CDC42* (Wu et al., 2015), expression of this internally tagged *CDC42* allele from its native promoter as the sole source of Cdc42 does not cause temperature sensitivity, and cells are fully viable at 37°C, though not at 39°C (Fig. S1 A). Live-cell imaging of this strain reveals the expected localization of Cdc42 at sites of polarized growth (Adams et al., 1990; Etienne-Manneville, 2004; Fig. 1 A). However, in addition to its expected localization, Cdc42-mCherry^{sw} showed a novel subcellular localization in 23% ± 6.9% of vegetatively growing cells (Fig. 1 B). These cells contained a single Cdc42 spot in the mother, in the bud, or in both the mother and bud, and sometimes the spot translocated from the mother to the bud (Fig. S1, B and C; and Video 1).

In an effort to identify the function of this spot, we first surveyed subcellular structures with which the spot might be associated by examining strains coexpressing endogenously tagged fluorescent organelle markers. We observed that the Cdc42 spot is associated with the vacuole in 100% of cases (Fig. 1 C), where it is either completely overlapping with or proximal to the vacuolar membrane, which we visualized using Vph1-GFP (Fig. S2 A). Additionally, we saw that the Cdc42 spot is proximal to the ER (marked by GFP-HDEL) 84.6% ± 6.9% of the time (Fig. 1 C and Fig. S2 B). As the Cdc42 spot is associated with the vacuole 100% of the time, it is at the nucleus-vacuole junction when we observe the spot proximal to the nuclear ER. Because this spot is associated with the vacuole, we attempted to determine whether it associates with multi-vesicular bodies (MVBs), because they associate with the vacuole. Markers that uniquely identify MVBs do not exist. However, MVBs become enriched and clustered in cells that overexpress the Rab5 homologue Vps21 (Adell et al., 2014). We reasoned that if Cdc42 is associated with clusters of MVBs, the appearance of the Cdc42 dots might change or their maximum intensity might increase. However, we did not see a difference in the appearance or maximum intensity of the Cdc42 spot between wild-type cells and cells overexpressing *VPS21* (Fig. S1 D). This analysis and attempts at correlative light microscopy electron microscopy (not shown) were inconclusive. Having identified a new subcellular Cdc42 localization at the vacuole and ER, we next wanted to determine if there is a function associated with the Cdc42 spot.

Because Cdc42 had previously been implicated in vacuole function (Eitzen et al., 2001; Müller et al., 2001) but never in ER function, we decided to focus on the function of ER-associated Cdc42. We therefore analyzed the dynamic behavior of the ER-associated spot relative to the ER membrane. Association of the Cdc42 spot with the nuclear envelope appears to be restricted to certain parts of the cell cycle, as we observed that it is associated with the nuclear envelope 82% of the time in unbudded cells and 90% of the time in cells undergoing cytokinesis (Fig. 1 D). Cdc42 localization to the nuclear envelope appeared to be random in budding cells, as 50% of Cdc42 spots were found on the ER in this cell cycle stage (Fig. 1 D). Live-cell imaging revealed that the Cdc42 spot often appears at the bottleneck region of the nuclear filament in cells undergoing nuclear fission. We observed that throughout the duration of nuclear fission, the Cdc42 spot remained near the base of the neck of the dividing nuclear envelope, whose outer membrane is continuous with the ER and thereby is marked by GFP-HDEL (Fig. 1 E, Video 2, Video 3, and Fig. S1 D). We observed the spot at the base of the nuclear filament 68% of the time in cells undergoing nuclear fission (Fig. 1 D) and observed that the spot could associate with the nuclear envelope during nuclear fission in either the mother cell or the bud, or in both (Fig. S1 F). In cells not undergoing nuclear fission, we observed a similar behavior of the spot at the base of ER tubules undergoing fission. Time lapse imaging of cells that exhibit fission of ER tubules emanating from the nucleus showed the Cdc42 spot localizing to the base of the ER tubule neck before, during, and after the fission event (Fig. 1 F and Video 2). These ER tubule fission events at the nuclear envelope were rare and difficult to capture.

The Cdc42 spot not only appears at sites of nuclear and ER membrane remodeling but also at vacuolar membrane remodeling. The Cdc42 spot can be observed at the vertices of fusing vacuoles, remaining at the convergence points until the vacuole fragments have fully fused (Fig. S2 C and Video 4), lending further evidence of a potential membrane-remodeling function for Cdc42. Having identified a novel subcellular localization of Cdc42 to organelles undergoing membrane remodeling, we next sought to determine if Cdc42 appears at these sites with proteins known to reshape intracellular membranes.

The ESCRT-III proteins have previously been found to remodel the same organelles that we found colocalized with Cdc42, so we tested whether Cdc42 and the ESCRT-III proteins are involved in the same membrane-remodeling process. The ESCRT family of proteins are membrane-deforming proteins known to function at endosomes and vacuoles (Zhu et al., 2017) and are also involved in sealing of discontinuities in the nuclear envelope (Webster et al., 2016; Gu et al., 2017; Vietri et al., 2015; Olmos et al., 2016). We first examined the subcellular localization of Chm7, an ESCRT-III-like protein that functions in nuclear envelope sealing in fission (*S. pombe* and *S. japonicus*) and budding yeast (Webster et al., 2016; Gu et al., 2017; Lee et al., 2020) and whose mammalian homologue CHMP7 functions in nuclear envelope reformation and sealing in animal cells (Olmos et al., 2016; Penfield et al., 2020; Vietri et al., 2015). As previously reported, we also found that Chm7 localizes to a single spot in a subpopulation of cells (Webster et al., 2016), with the Chm7

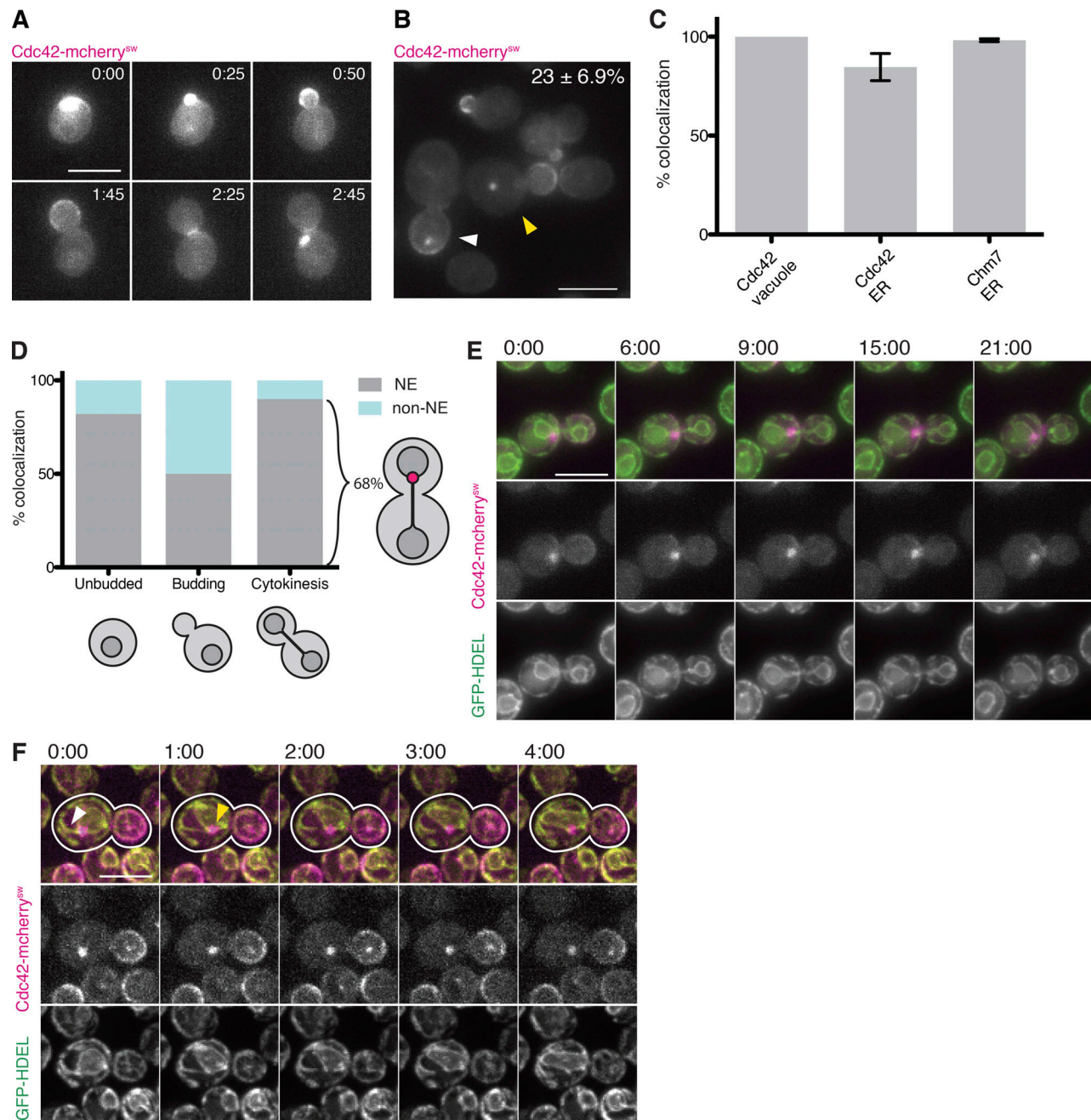


Figure 1. Cdc42-mCherry^{SW} localizes to a single spot at sites of ER remodeling in a subpopulation of cells. (A) Montage of wide-field epifluorescence time lapse imaging of cells endogenously expressing Cdc42-mCherry^{SW} during polarized cell growth. Cells were imaged in early-log phase in minimal imaging media at 23°C–25°C. 3-μm maximum-intensity projection at 0.5-μm steps. (B) Field of view of same strain as in A showing two examples of the 23% ± 6.9% of cells with Cdc42 spots (±SD; *n* = 1,527; four trials). White arrowhead indicates bud containing Cdc42 spot, and yellow arrowhead indicates a budding mother containing Cdc42 spot. (C) Quantification of frequency of Cdc42 or Chm7 spot colocalized with the vacuole or ER. Two trials for each, mean ± SD. Cdc42 and vacuole: 100% ± 0%; *n* = 27. Cdc42 and ER: 84.6% ± 6.9%; *n* = 170. Chm7 and ER: 98.2% ± 0.72%; *n* = 165. (D) Frequency of Cdc42 localization to the nuclear envelope during unbudded, budding, and cytokinesis stages of the cell cycle. Unbudded: 82%, *n* = 34; Budding: 50%, *n* = 38; Cytokinesis: 90%, *n* = 20. Also depicts percentage of cells undergoing nuclear fission within cytokinetic cells (*n* = 18) with Cdc42 spot at bottleneck region of nuclear filament undergoing nuclear fission (68%). (E) Montage of confocal spinning-disk movie stills of the same cells as in A undergoing nuclear fission. 3-μm maximum-intensity projections at 0.5-μm steps. (F) Montage of confocal spinning-disk movie stills of cells endogenously expressing Cdc42-mCherry^{SW} (magenta) and GFP-HDEL (green) undergoing fission of ER tubule emanating from the nucleus. White arrowhead in first frame indicates ER tubule, and yellow arrowhead in second frame indicates site of severed ER tubule on the nuclear ER. 2-μm maximum-intensity projections at 0.5-μm steps. All scale bars, 5 μm.

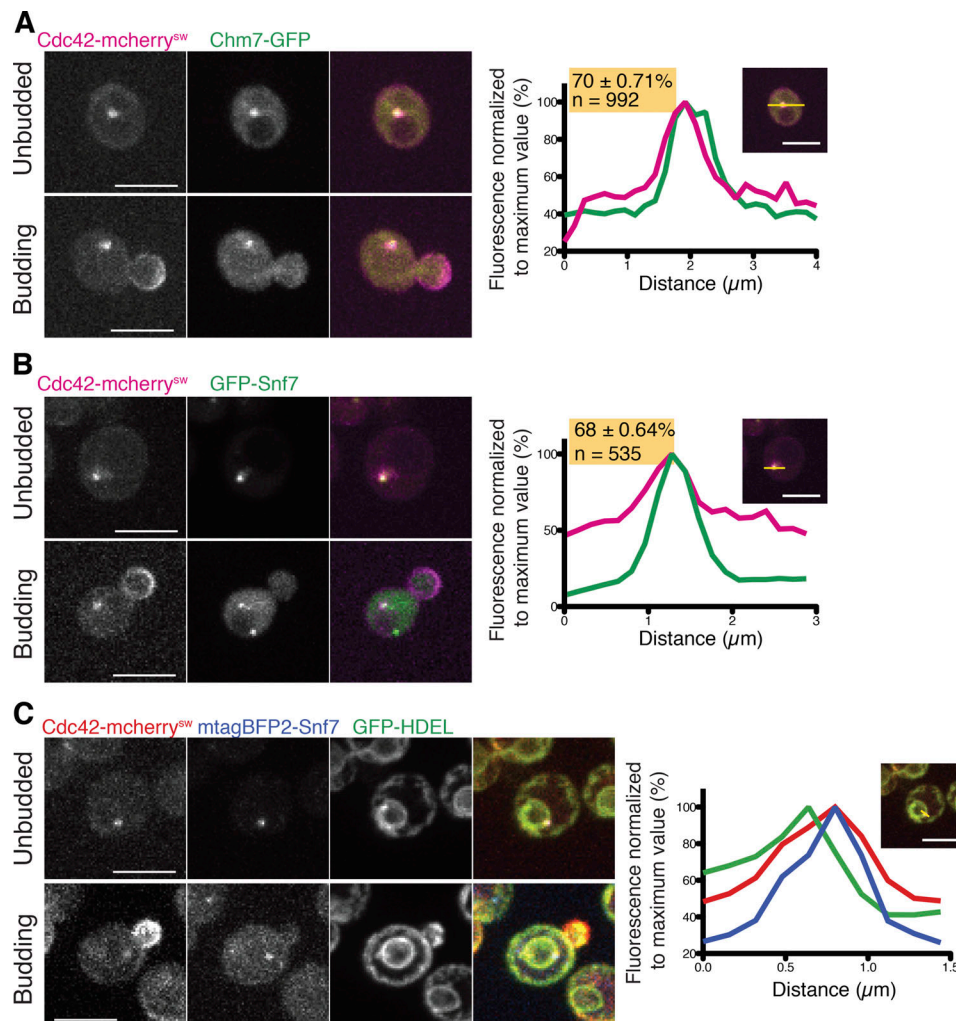


Figure 2. Cdc42 colocalizes with ESCRTs in vivo. (A) Confocal spinning-disk still images of cells endogenously expressing Cdc42-mCherry^{SW} (magenta) and Chm7-GFP (green) in unbudded (top panel) or budded (lower panel) cells. Plot of normalized fluorescence intensity profiles of Chm7-GFP (green) and Cdc42-mCherry^{SW} (magenta) along yellow line shown in inset image. Cells that contain both Cdc42 spot and Chm7 spot where both are colocalized = $70 \pm 0.71\%$ (SD; $n = 992$; two trials). **(B)** Confocal spinning-disk stills of cells endogenously expressing Cdc42-mCherry^{SW} (magenta) and GFP-Snf7 (green) in unbudded (top panel) or budded (lower panel) cells. Plot of normalized fluorescence intensity profiles of GFP-Snf7 (green) and Cdc42-mCherry^{SW} (magenta) along yellow line shown in inset image. Cells that contain both Cdc42 spot and Snf7 punctae, where they are colocalized = $68 \pm 0.64\%$ (SD; $n = 535$; two trials). **(C)** Confocal spinning-disk stills of cells endogenously expressing Cdc42-mCherry^{SW} (red), GFP-HDEL (green), and mtgBFP2-Snf7 (blue) in G1 phase (top panel) or budding (lower panel). Plot of normalized fluorescence intensity profiles of Cdc42 (magenta), ER (green), and Snf7 (blue) along yellow line shown in inset image. All images are 2- μ m maximum-intensity projections at 0.5- μ m steps. All scale bars, 5 μ m.

spot at the ER $98.2 \pm 0.7\%$ of the time (Fig. 1 C). In cells harboring both Cdc42 and Chm7 foci, $\sim 70\%$ of the Cdc42 spots colocalized with the Chm7 spot (Fig. 2 A). We also examined the subcellular localization of Snf7, an ESCRT-III protein that functions with Chm7 in the sequestration of defective nuclear pore complexes (NPCs) in budding yeast (Webster et al., 2014) and whose mammalian homologue CHMP4B is involved in nuclear envelope sealing in animal cells (Olmos et al., 2015). Unlike Chm7 and Cdc42, Snf7 formed a varying number of intracellular foci. Importantly, in cells containing a Cdc42 spot and at least one GFP-Snf7 spot, $\sim 70\%$ of Cdc42 spots colocalized with a GFP-Snf7 spot (Fig. 2 B). To determine whether the Cdc42 spot with Snf7 is the same structure as the Cdc42 spot near the ER (Fig. 1, E and F; and Fig. S2 B), we generated a strain expressing Cdc42-mCherry^{SW}, GFP-HDEL, and mtgBFP2-Snf7 for three-color live-

cell imaging. We observed that ER-proximal Cdc42 spots also contained Snf7 (Fig. 2 C), suggesting that they are the same structure.

Live imaging of Chm7 and Snf7 suggested that they, like Cdc42, are involved in a putative ER membrane-remodeling process. Like the Cdc42 spot, we observed instances of the Chm7 spot and Snf7 punctae localizing to the ER bottleneck areas of nuclear envelope fission (Fig. 3, A and B). This localization behavior is consistent with numerous studies detailing ESCRT-III proteins' preferences for high-curvature membranes, particularly necks and holes (Cashikar et al., 2014; Lee et al., 2015; De Franceschi et al., 2019; Penfield et al., 2020; McCullough et al., 2015). Three-color live-cell imaging revealed that Cdc42 and Snf7 colocalize to the same peri-nuclear structure that, in cells undergoing cytokinesis, appears to migrate to the base of

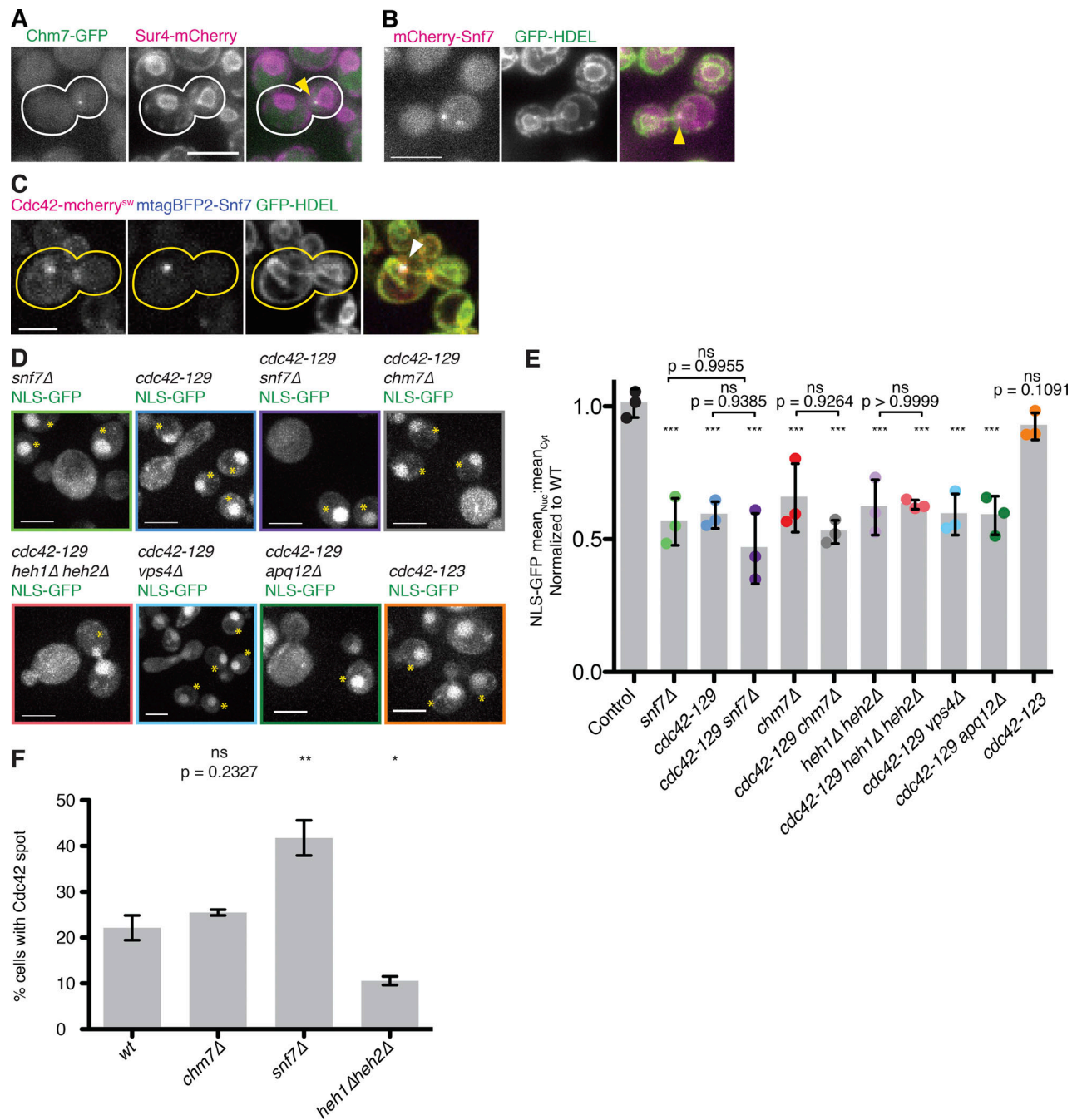


Figure 3. Cdc42 functions in the same NE sealing pathway as ESCRT and LEM proteins. (A) Stills from epifluorescence movies of cells endogenously expressing Chm7-GFP (green) and Sur4-mCherry (magenta) to mark the nuclear envelope. Yellow arrowhead indicates Chm7 spot at postfission nuclear membrane. **(B)** Stills from epifluorescence movies of cells endogenously expressing mCherry-Snf7 (magenta) and GFP-HDEL (green) to mark the ER. Yellow arrowhead indicates Snf7 punctum at base of ER tubule neck undergoing nuclear fission. **(C)** Confocal spinning-disk still of a cell endogenously expressing Cdc42-mCherry^{SW} (red), GFP-HDEL (green), and mtagBFP2-Snf7 (blue) undergoing nuclear fission. White arrowhead indicates Snf7 and Cdc42 structure on ER membrane. **(D)** Confocal spinning-disk micrographs of indicated mutant strains, with wild-type (wt) cells (marked with yellow asterisks) in the same field of view. **(E)** Quantification of each mutant's mean nuclear:cytosolic GFP fluorescence intensity normalized to that of wild-type cells in the same field of view. Colored dots report means from individual trials. Asterisks denote statistical significance compared with control after one-way ANOVA ($F = 10.74$), followed by Sidak's multiple comparison test to determine P values between bracketed strains. Three trials were conducted for each mutant. n , mean \pm SD are as follows: control $n = 434$ (wt $n = 332$), 1.02 ± 0.05 ; *snf7Δ* $n = 286$ (wt $n = 224$), 0.57 ± 0.09 ; *cdc42-129* $n = 115$ (wt $n = 266$), 0.60 ± 0.05 ; *cdc42-129 snf7Δ* $n = 293$ (wt $n = 633$), 0.47 ± 0.13 ; *chm7Δ* $n = 422$ (wt $n = 443$), 0.66 ± 0.13 ; *cdc42-129 chm7Δ* $n = 233$ (wt $n = 443$), 0.53 ± 0.04 ; *heh1Δheh2Δ* $n = 366$ (wt $n = 169$), 0.63 ± 0.10 ; *cdc42-129 heh1Δheh2Δ* $n = 229$ (wt $n = 192$), 0.64 ± 0.02 ; *cdc42-129 vps4Δ* $n = 92$ (wt $n = 137$), 0.60 ± 0.08 ; *cdc42-129 apq12Δ* $n = 181$ (wt $n = 446$), 0.60 ± 0.08 ; *cdc42-123* $n = 95$ (wt $n = 141$), 0.93 ± 0.05 . **(F)** Quantification of wild-type, *chm7Δ*, *snf7Δ*, or *heh1Δheh2Δ* mutant cells with a Cdc42 spot. wt: $23\% \pm 6.9\%$, four trials, $n = 1,527$. *chm7Δ*: $25\% \pm 0.6\%$, two trials, $n = 1,120$. *snf7Δ*: $42\% \pm 3.8\%$, two trials, $n = 1,136$. *heh1Δheh2Δ*: $11\% \pm 0.9\%$, $n = 752$. *, $P \leq 0.05$; **, $P \leq 0.01$; ***, $P \leq 0.001$. **(A–C)** Shown are 2- μ m maximum-intensity projections at 0.5- μ m steps. **(D)** Shown is 11- μ m maximum-intensity projection at 0.5- μ m steps. All cells in this figure were grown to log phase in minimal imaging media at 23°C–25°C. All scale bars, 5 μ m. ns, not significant. Cyt, cytosol; Nuc, nucleus.

the nuclear filament of a dividing nucleus (Fig. 3 C and Video 5). These observations suggest that both Cdc42 and Snf7 function together at ER fission sites. These live-cell imaging observations point to a membrane-remodeling function for Cdc42 and, together with the colocalization with ESCRT proteins, suggest that Cdc42 functions with Snf7 and Chm7 at the ER membrane.

Because ESCRT proteins have been extensively documented to function in nuclear envelope sealing in budding yeast, fission yeast (*S. pombe* and *S. japonicus*), nematode, and mammalian cells (Webster et al., 2014, 2016; Gu et al., 2017; Lee et al., 2020; Penfield et al., 2020; Vietri et al., 2015; Olmos et al., 2015), we reasoned that Cdc42 may coordinate with Chm7 and Snf7 to seal the hole left behind in the nuclear envelope after ER tubule fission from the nuclear envelope. This possibility is consistent with findings from previous studies in which ESCRT-III depletion in mammalian cells disrupts the annular fusion of the re-assembling nuclear envelope after mitosis, ultimately causing a reduction in the postmitotic nucleocytoplasmic partitioning of a NLS-GFP probe (Olmos et al., 2015). A similar leaky nucleus phenotype occurs in *chm7Δ* budding yeast and *cnp7Δ* *S. japonicus* fission yeast, where the deletion of *CHM7* and *cnp7*, respectively, leads to a decrease in nuclear/cytosolic mean NLS-GFP fluorescence ratio at 37°C (Webster et al., 2016; Lee et al., 2020).

To determine whether *CDC42* is also required for nuclear envelope sealing, we searched for *cdc42* mutants with a leaky nucleus phenotype and identified the *cdc42-129* allele, which contains a single point mutation, V36T, that perturbs a yet-to-be-identified Cdc42 function (Kozminski et al., 2000). At the restrictive temperature of 37°C, the majority of *cdc42-129* mutants are severely misshapen, often containing one or more elongated buds, and a smaller fraction of *cdc42-129* mutants display a terminal phenotype of unbudded, multinucleated cells. Additionally, at the restrictive temperature, *cdc42-129* mutants exhibit sustained polarized Cdc42p and actin at sites of bud growth. It is thought that because the *cdc42-129* allele is recessive, this mutant may have lost the ability to generate a signal that promotes the appropriately timed redistribution of the actin cytoskeleton (Kozminski et al., 2000). Using the NLS-GFP reporter assay, we found that the temperature-sensitive *cdc42-129* allele causes a leaky nucleus phenotype at the restrictive temperature of 37°C, phenocopying *chm7Δ* (Webster et al., 2016; Fig. 3, D and E; Fig. S2 D; and see Table S1, Table S2, and Table S3). The *cdc42-129 chm7Δ* double mutant does not have an exacerbated phenotype and also displays the same severe morphological defects as the *cdc42-129* single mutant, suggesting that these two proteins function in the same pathway. Similar to *chm7Δ*, *snf7Δ* cells also have leaky nuclei, and combining this deletion with *cdc42-129* gave the same phenotype as the single mutants (Fig. 3, D and E; Fig. S2 D; and see Table S1).

To determine whether the leaky nucleus phenotype is the result of a specific function of Cdc42 and is not caused by a pleiotropic effect of general Cdc42 dysfunction (such as defects in actin assembly), we tested for leaky nuclei in *cdc42-123*, another temperature-sensitive *cdc42* mutant that was previously characterized as having defects in vacuole fusion (Müller et al., 2001). At the restrictive temperature, we observed the previously reported fragmented vacuole phenotype for *cdc42-123*, but

not for *cdc42-129* mutants (Fig. S3 A). Furthermore, we did not observe a leaky nuclei phenotype for *cdc42-123* mutants at the restrictive temperature as we did for *cdc42-129* mutants (Fig. 3, D and E; Fig. S2 D; and see Table S1). Thus, nuclear envelope sealing appears to be a specific Cdc42 function in the same pathway as the ESCRT-III proteins Snf7 and Chm7 in nuclear envelope sealing. However, we cannot eliminate the possibility that perturbations to actin regulation in the *cdc42-129* mutant caused the nuclear envelope sealing defects that we observed at the restrictive temperature.

Further molecular genetic analysis revealed that Cdc42 functions with the LEM-family proteins Heh1/Heh2 and the integral membrane protein Apq12 in nuclear envelope resealing. Chm7 and Snf7 function with the LEM protein Heh2 and its paralog Heh1 in NPC quality control and nuclear envelope sealing in budding yeast, and *CHM7* genetically interacts with *APQ12* (Webster et al., 2014, 2016). In addition, in fission yeast and human cells, the LEM-family protein LEM2 recruits CHMP7 during nuclear envelope closure (Gu et al., 2017), and in budding yeast, the Lem2 orthologue Heh1 is also required for the recruitment of Chm7 to the nuclear envelope (Thaller et al., 2019).

To determine if Cdc42 is a component of this LEM-ESCRT-III protein complex that functions in nuclear envelope sealing, we tested for genetic interactions between mutant alleles of *CDC42* and *HEH1/HEH2*. As reported previously, we found that *heh1Δheh2Δ* mutants have leaky nuclei (Webster et al., 2014; Fig. 3, D and E; Fig. S2 D; and see Table S1). Combining these mutations with the *cdc42-129* mutation did not result in a more severe phenotype, and the double mutant displays the same severe morphological defects as the *cdc42-129* mutant (Fig. 3 D, E; Fig. S2 D; and see Table S1), suggesting that all three proteins function in the same pathway for this cellular function. Our genetic analyses suggest that *CDC42* functions in the same pathway with *HEH1*, *HEH2*, *SNF7*, and *CHM7* in nuclear envelope sealing. Because Heh1/Heh2, Chm7, and Snf7 have been reported to function in a previously described quality control pathway that surveils NPC assembly (Webster et al., 2014, 2016), we next tested whether Cdc42 functions in this LEM-ESCRT-III-mediated NPC quality control pathway.

Cells defective for NPC assembly employ a pathway that involves Heh1/Heh2, Chm7, and Snf7 to sequester the aberrant NPCs in a perinuclear compartment termed the SINC (Storage of Improperly assembled NPCs; Webster et al., 2014, 2016). SINC can be visualized by optical microscopy as clusters of NPC proteins (termed Nups) on the periphery of the nucleus. The ESCRT-III components that play a role in this pathway, such as Chm7 and Snf7, localize with or near the SINC (Webster et al., 2016, 2014). Additionally, ESCRT-III mutants, such as *snf7Δ* mutants, have increased frequency of SINC formation (Webster et al., 2014). We examined whether the Cdc42 spot colocalizes with the SINC in *snf7Δ* cells, which display both leaky nucleus phenotype and SINC phenotype (Webster et al., 2014; Fig. 3, D and E; Fig. S2 D; Fig. S3 B; and see Table S1). Unlike Chm7, which was found to colocalize with Nup clusters (i.e., the SINC; Webster et al., 2016), the Cdc42 spot does not colocalize with Nup188-GFP clusters in *snf7Δ* cells (Fig. S3 D and Video 6). To determine if the NE sealing pathway is distinct from the NPC

quality control pathway that generates the SINC, we tested whether the presence of the SINC predicts a leaky nuclei phenotype. We observed no significant difference in the distribution of NLS-GFP nucleus/cytoplasm ratios in cells that contain a SINC and those that do not, suggesting that there is no causal relationship between these phenotypes (Fig. S3 C). We conclude that Cdc42 functions with Heh1/Heh2, Chm7, and Snf7 in an NE sealing pathway that is distinct from an NPC surveillance pathway, which also involves Heh1/Heh2, Chm7, and Snf7. We next sought to elucidate the molecular mechanisms underlying Cdc42 function in this pathway.

To determine whether the formation of the Cdc42 spot on the nuclear envelope requires any of the other components in the LEM-ESCRT-III-mediated NE sealing pathway, we scored the percentage of cells containing the Cdc42 spot in *heh1Δheh2Δ*, *chm7Δ*, and *snf7Δ* mutants. *chm7Δ* mutants displayed no change in the percentage of cells containing a Cdc42 spot, suggesting that it is not required for the formation of the Cdc42 spot (Fig. 3 F). However, *heh1Δheh2Δ* mutants displayed a significant decrease in the percentage of cells containing a Cdc42 spot, suggesting that Heh1/Heh2 are required for the formation of the Cdc42 spot (Fig. 3 F). Interestingly, *snf7Δ* mutants had an increase in the percentage of cells that contain a Cdc42 spot, suggesting that it plays a role in the turnover or disassembly of the Cdc42 spot (Fig. 3 F). Thus, the formation of the Cdc42 spot on the NE appears to be regulated by Heh1/Heh2 and Snf7. We next sought to determine whether Cdc42 regulates the components of the LEM-ESCRT-III-mediated NE sealing pathway.

How the ESCRT and LEM-family proteins are regulated during nuclear envelope sealing function is not yet known, so we investigated whether Cdc42 plays a regulatory role in this pathway. Many of the ESCRT-III proteins contain an auto-inhibitory regulatory C-terminal region whose de-repression leads to polymerization into active oligomers (Cashikar et al., 2014; Hanson et al., 2008; Henne et al., 2012; Shen et al., 2014; Tang et al., 2015). The disassembly of “open” ESCRT-III oligomers can be induced by the association with the type 1 AAA⁺ ATPase Vps4; the strength of the binding affinities of different ESCRT-III proteins for Vps4 are directly correlated with how well they are disassembled. While the mechanisms underlying Vps4-mediated disassembly of ESCRT-III proteins CHMP1 (Stuchell-Brereton et al., 2007), CHMP2 (Stuchell-Brereton et al., 2007; Obita et al., 2007), CHMP6 (Kieffer et al., 2008), and IST1 (Guo and Xu, 2015), which associate with each other tightly, are known, how Vps4 disassembles weakly interacting or noninteracting ESCRT-III proteins, including CHMP4/Snf7, is not known, though it has been proposed that accessory proteins that bind both ESCRT-III and Vps4 might facilitate Vps4-mediated disassembly (Schöneberg et al., 2017).

To explore whether Cdc42 plays a direct or accessory role in Vps4-mediated ESCRT filament disassembly, we first determined whether Vps4 is present at sites of Cdc42's nuclear function. Using a fully functional endogenous Vps4-3xHA-GFP (Adell et al., 2017), we observed Vps4 punctae at the base of nuclear filaments in cells undergoing nuclear fission (Fig. 4 A) and also observed that Vps4 punctae colocalize with the Cdc42 spot in 70% of cells harboring a Cdc42 spot (Fig. 4 B).

Additionally, previous studies have shown that *vps4Δ* mutants have leaky nuclei (Webster et al., 2014). We determined that combining *vps4Δ* and *cdc42-129* does not exacerbate the NLS-GFP phenotype and that this double mutant also displays the same severe morphological defects as the *cdc42-129* mutant, implicating that Vps4 is a component of the Cdc42-LEM-ESCRT-III-mediated NE sealing pathway (Fig. 3, D and E; Fig. S2 D; and see Table S1). Vps4 was not necessary for the formation of the Cdc42 spot as *vps4Δ* cells had a similar percentage of Cdc42 spots as wild-type cells ($25\% \pm 0.01\%$, two trials; $n = 1,055$). Having established that Cdc42 colocalizes with the machinery required for ESCRT-III filament disassembly, we next determined if Cdc42 plays a role in Snf7 recruitment to Vps4 and/or Snf7 filament disassembly.

To determine if Cdc42 is required for recruitment of Snf7 to Vps4, we tested whether Snf7 and Vps4 colocalization was impaired in *cdc42-129* mutants. We observed no change in the levels of colocalization between wild-type cells and *cdc42-129* mutants, indicating that Snf7 recruitment to Vps4 is not disrupted by this mutant (Fig. S3, E and F). Though Cdc42 does not appear to mediate a Snf7-Vps4 union, it may function as an accessory protein required for Vps4-mediated Snf7 filament disassembly. To determine if the Cdc42 spot is at sites of Snf7 filament disassembly, we examined the dynamic behavior of the Cdc42 spot and colocalized Snf7 punctae using high time-resolution live-cell imaging. While most of the colocalized Cdc42 and Snf7 spots persisted throughout the duration of imaging sessions, we were able to observe a few instances where a Snf7 spot disassembled while the colocalized Cdc42 signal remained persistent. These rare observations prompted us to hypothesize that the Cdc42 spot functions to promote disassembly of Snf7 oligomers in vivo (Fig. 4 C).

To explore the possibility that Cdc42 mediates Vps4-mediated Snf7 filament disassembly through a direct interaction, we determined if Cdc42 directly binds to ESCRT-III proteins. Using a GST pulldown assay with purified proteins, we found that Cdc42 interacts with full-length Chm7, the putative “open” form of Chm7 (Chm7^{open}), and the open form of Snf7 (Snf7^{open}), but not to the full-length “closed” form of Snf7 (Webster et al., 2016; Saksena et al., 2009; Fig. 4 D). Additionally, we found that the *cdc42-129* allele's protein product, a V36T point mutant, has a decreased binding affinity for Snf7^{open} (Fig. S3 G). These in vitro binding studies suggest that Cdc42 associates with open active Snf7 in vivo. These observations considered with the live-cell imaging results suggest that Cdc42 binding to Chm7 and/or Snf7 might facilitate disassembly of Snf7 filaments by Vps4. We next analyzed the in vivo effects of the Cdc42^{V36T} mutant's (*cdc42-129*) decreased binding affinity for Snf7.

To determine whether Cdc42 is required for Snf7 oligomer disassembly in vivo, we examined by fluorescence microscopy the number of mCherry-Snf7 punctae in *cdc42-129* mutants. To avoid bias in defining the parameters for punctae selection, we measured the overall frequency distribution of pixel intensities of mCherry-Snf7 signal at the medial focal plane (see Materials and methods). Compared with wild-type cells, *cdc42-129* mutants had more high-intensity mCherry-Snf7 pixels than the control, and this phenotype was specific to this allele as *cdc42-123*

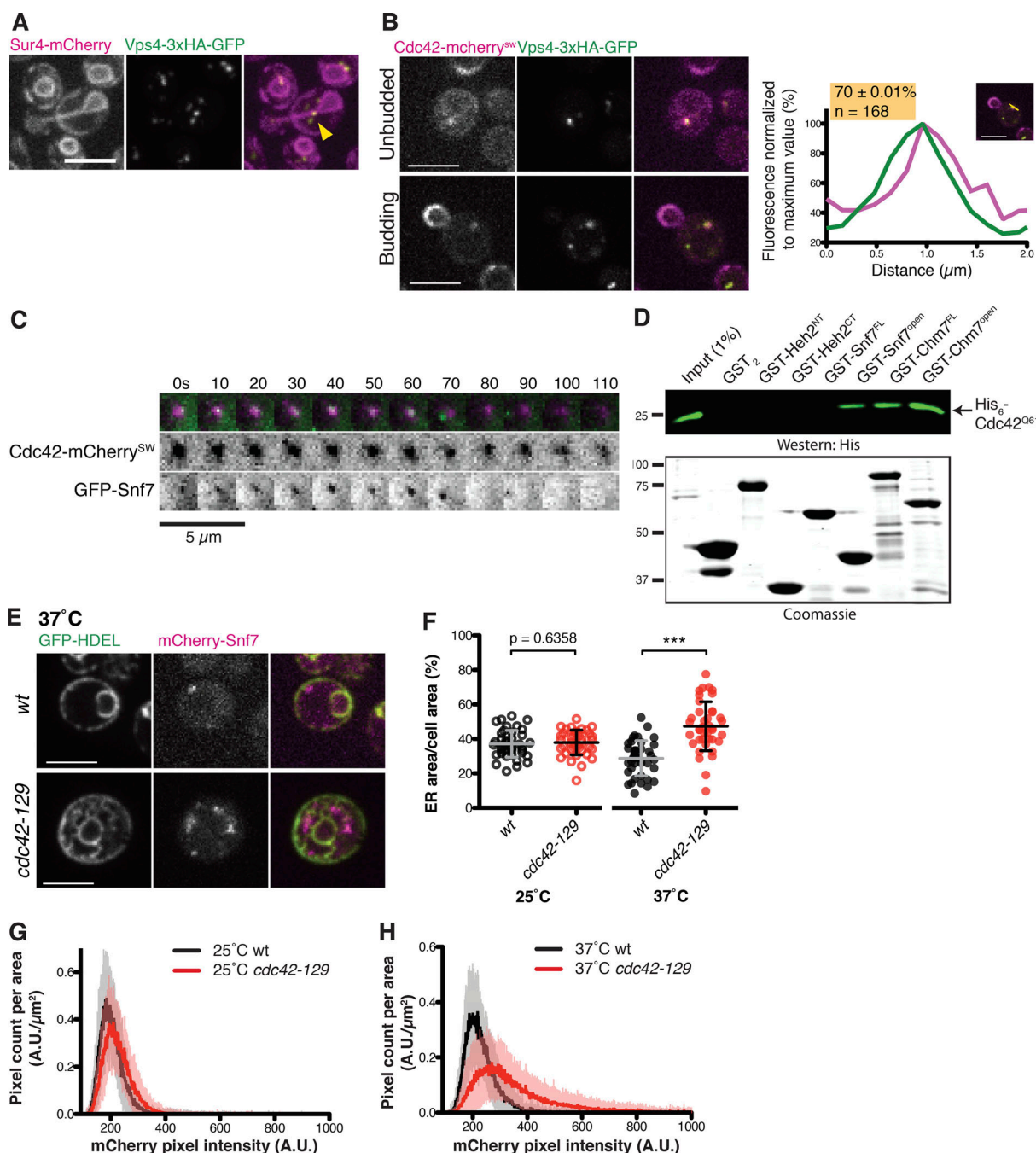


Figure 4. Cdc42 is at sites of Snf7 disassembly, and its disruption leads to Snf7 aggregates and ER tubule extensions from the nuclear envelope.

(A) Still images from epifluorescence movies of cells endogenously expressing Vps4-3xHA-GFP (green) and Sur4-mCherry (magenta) to mark the nuclear envelope. Yellow arrowhead indicates Vps4 spot at base of nuclear filament. **(B)** Confocal spinning-disk still images of cells endogenously expressing Cdc42-mCherry^{SW} (magenta) and Vps4-3xHA-GFP (green) in unbudded (top panel) or budded cell (lower panel). Plot of normalized fluorescence intensity profiles of Vps4-3xHA-GFP (green) and Cdc42-mCherry^{SW} (magenta) along yellow line shown in inset image. Cells that contain both Cdc42 spot and Vps4 spot, where both are colocalized = 70.6% \pm 0.01% (SD; n = 168). **(C)** Montage of stills from confocal spinning-disk movie of a Cdc42 spot (magenta) and Snf7 (green) punctum. Time is in seconds. **(D)** GST-fusions of Heh2^{C-terminal}(CT), Heh2^{N-terminal}(NT), Chm7, or Snf7 fragments or full-length protein (Coomassie, lower panel) were immobilized on GST-beads as bait and incubated with purified His₆-Cdc42^{Q61L} (constitutively GTP bound) as prey (detected by Western blot, top panel). **(E)** Confocal spinning-disk micrographs of wild-type (wt; top panel) and *cdc42-129* (bottom panel) cells expressing GFP-HDEL (green) to mark ER and mCherry-Snf7 (magenta) grown to early-log phase in minimal media and shifted to 37°C for 6 h. Single (medial) focal plane. **(F)** Quantification of percentage cell area occupied by ER for same strains shown in E. Open circles indicate wild-type (black) and *cdc42-129* mutant (red) strains imaged at the permissive temperature (25°C), and closed circles at the restrictive temperature (37°C). wt 25°C: two trials, n = 40, 37.1 \pm 7.8; *cdc42-129* 25°C: two trials, n = 40, 37.9 \pm 7.2; wt 37°C: two trials, n = 40, 28.7 \pm 10.2; *cdc42-129* 37°C: two trials, n = 40, 47.3 \pm 14.2. mean \pm SD. Asterisks denote statistical significance compared with control using Student's *t* test. ***, *P* \leq 0.001. **(G)** Quantification of mCherry-Snf7 puncta of same strain shown in E grown to early-log phase in minimal media at 25°C, as a frequency distribution of the fluorescence intensity of each pixel in a cell normalized to cell area (micrometer squared). Two trials, n = 40. **(H)** Quantification of mCherry-Snf7 puncta of same strain shown in E grown to early-log phase in minimal media then shifted to 37°C for 6 h. Two trials, n = 40. All scale bars, 5 μm .

mutants did not exhibit more high-intensity mCherry-Snf7 pixels (Fig. S3 H). This increase in the amount of large Snf7 assemblies suggests that *cdc42-129* mutants have defects in Snf7 disassembly and turnover (Fig. 4, E, G, and H). Thus, Cdc42 appears to be required for the disassembly of Snf7 filaments, possibly through a direct interaction, but not for Snf7 recruitment to Vps4.

Our initial characterization of the Cdc42 spot revealed a curious localization to the site of fission of an ER tubule that bridges the nuclear and cortical ER (Fig. 1 F). The yeast ER network is composed primarily of cortical ER and nuclear ER, with the cytoplasmic space generally devoid of ER tubules (Preuss et al., 1991). Furthermore, cortical ER morphology, mobility, and inheritance in budding yeast require the actin cytoskeleton, which is regulated by Cdc42 (Du et al., 2004; Estrada et al., 2003; Prinz et al., 2000; Fehrenbacher et al., 2002; Wiederkehr et al., 2003). Therefore, our rare observation of the Cdc42 spot at sites of ER tubules undergoing fission prompted us to examine the ER morphology of the *cdc42-129* mutant. We observed that *cdc42-129* mutants exhibit an ER phenotype in which the cytoplasmic space between the nuclear ER and the cortical ER is filled with a network of ER tubules emanating from the nuclear ER (Fig. 4, E and F). This phenotype is specific to the *cdc42-129* allele, as *cdc42-123* mutants do not exhibit cytoplasmic ER tubules, though the *cdc42-123* mutant does exhibit excess cortical ER (Fig. S3, I and J). Because ER morphology can be affected by disruptions to actin (Prinz et al., 2000; Fehrenbacher et al., 2002), the ER phenotype observed in *cdc42-129* mutants may be caused by Cdc42 dysregulation of actin assembly. This phenotype suggests that, in addition to sealing holes in the nuclear envelope, Cdc42 is also involved in maintaining the architecture of the ER, possibly by regulation of actin reorganization at sites of ER remodeling. Together with the previous section's findings, these fluorescent microscopy findings support the idea that Cdc42 functions as a regulator of Snf7 disassembly, either directly or indirectly through the regulation of actin reorganization. In either case, the loss of Cdc42 regulation results in an increase in Snf7 filaments that cause disorganization of the nuclear envelope and ER.

We have uncovered novel functions of Cdc42 as a regulator of ESCRT-III disassembly during nuclear envelope sealing and in the maintenance of ER morphology. In budding yeast, fission yeast, and mammalian cells, loss of ESCRT-III and LEM function causes persistent holes in the nuclear envelope, ultimately leading to defective nucleocytoplasmic partitioning (Vietri et al., 2015; Olmos et al., 2015; Webster et al., 2014; Gu et al., 2017; Fig. 5 B). The same functional consequence occurs when the LEM-ESCRT complex fails to disassemble. Fission yeast lacking Vps4, and therefore exhibiting unrestricted ESCRT-III function, have persistent fenestrations, perinuclear ER stracks (karmellae), and disorganized tubular extensions of the nuclear envelope, culminating in the loss of nucleocytoplasmic compartmentalization (Gu et al., 2017; Fig. 5 C). In a similar vein, in budding yeast, VPS4 synthetically interacts with various ESCRT and nuclear envelope proteins to generate abnormal nuclear envelope phenotypes (Webster et al., 2014; Thaller et al., 2019). While the *cdc42-129* mutant exhibits a leaky nucleus phenotype

like *snf7Δ*, *chm7Δ*, and *heh1Δheh2Δ* mutants, it also displays increased Snf7 aggregates and sinuous tubular extensions from the nuclear envelope, reminiscent of the disorganized tubular extensions of the nuclear membrane observed in *vps4Δ* fission yeast (Gu et al., 2017). Cdc42 does not seem to be required for the recruitment of Snf7 filaments to Vps4 but is instead required for the disassembly of Snf7 filaments. These data suggest that Cdc42 regulates ESCRT-III disassembly, which is required for both nuclear envelope sealing and maintenance of proper ER architecture in budding yeast.

Because ER morphology, inheritance, and mobility are known to be regulated by actin reorganization in budding yeast (Du et al., 2004; Estrada et al., 2003; Prinz et al., 2000; Fehrenbacher et al., 2002; Wiederkehr et al., 2003) and because Cdc42 is a well-known regulator of actin assembly, we cannot eliminate a model wherein the ER architecture and NE sealing phenotypes observed in the *cdc42-129* mutant are the result of dysregulation of actin assembly. We therefore propose that Cdc42 functions in ESCRT-mediated nuclear envelope sealing as a regulator of ESCRT-III disassembly, where it appears to function with Vps4 to dismantle the ESCRT-LEM machinery at the nuclear envelope to seal holes in the nuclear envelope as well as maintain ER morphology (Fig. 5 A), either through direct ESCRT-III regulation or indirectly through actin assembly regulation at these sites.

Because Cdc42 preferentially binds to the open form of Snf7 and the protein product of the *cdc42-129* allele has a decreased affinity for Snf7, we speculate that Cdc42 may act as a cofactor to activate Vps4-mediated Snf7 filament disassembly through a direct binding interaction. We further propose that the Cdc42 spot is a transient body that forms at sites of holes in the nuclear envelope that develop as a result of nuclear fission or ER tubule fission and that the recruitment of Cdc42 to these holes is performed by Heh1/Heh2, as *heh1Δheh2Δ* mutants have fewer Cdc42 spots. Chm7 appears not to be involved in the recruitment of Cdc42, and we propose that it functions as an indispensable constituent of the ESCRT-III filament formed by Chm7 and Snf7. We propose that the Cdc42 spot disassembles upon the completion of annular fusion, cued by Snf7 filament disassembly, as *snf7Δ* mutants have an increased number of Cdc42 spots. Taken together, our live-cell imaging, biochemical, and genetic analyses provide evidence for a novel Cdc42 function in nuclear envelope sealing and ER remodeling as the first-identified regulator of ESCRT-III function in this process.

Materials and methods

Yeast strain generation and growth

All strains and the details of their construction are described in Table S2. Gene knockouts and C-terminal fluorescent protein fusions of endogenous genes were constructed using PCR-based integration of DNA cassettes derived from template plasmids as previously described (Longtine et al., 1998). N-terminal fusions were constructed using PCR-based integration of DNA cassettes generated using overlap extension PCR. The NLS-GFP strain was generated by integrating at the *LEU2* locus an NLS-3xGFP-containing plasmid, which was generously provided by

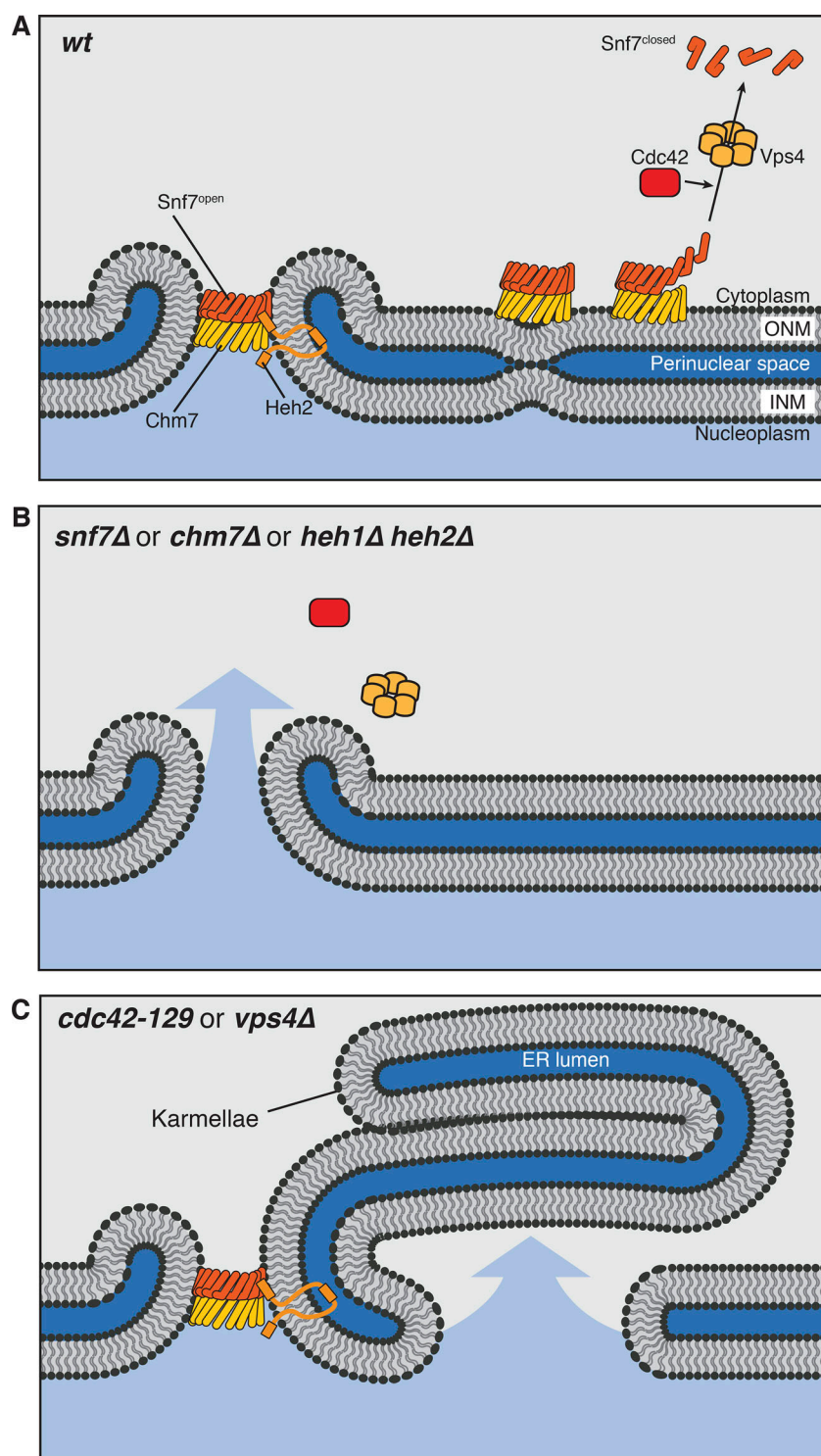


Figure 5. Cdc42, ESCRT-III, and Heh2 mutants share a leaky nucleus phenotype. (A) In normal cells, Heh2, Chm7, and Snf7 function at holes in the nuclear envelope to carry out annular fusion. ESCRT-III polymers are disassembled by Vps4, and we propose that Cdc42 is involved in the disassembly step by either directly contributing to Snf7 disassembly, activating Vps4 function, or cooperating with Vps4. **(B)** Mutants lacking components directly involved in annular fusion have holes in their nuclear envelopes left by nuclear fusion and ER fission events. **(C)** Cells lacking Vps4 and normal Cdc42 have unregulated ESCRT activity at the nuclear envelope. This causes the formation of nuclear karmellae and large holes in the nuclear envelope, leading to a defect in proper nucleo-cytoplasmic partitioning. ONM, outer nuclear membrane; INM, inner nuclear membrane.

Patrick Lusk (Yale University, New Haven, CT) (Webster et al., 2016), which is further described in Plasmids. The HDEL strain was generated by integrating at the *TPI1* locus a GFP-HDEL-containing plasmid, which was generously provided by Laura Lackner (Northwestern University, Evanston, IL)/Jodi Nunnari (University of California, Davis, Davis, CA)/Randy Schekman (University of California, Berkeley, Berkeley, CA; personal communication) and is further described in Plasmids. The *CDC42-mCherry^{SW}::HIS3* strain was constructed by

transforming a *cdc42Δ::LEU/CDC42* diploid strain with a double-stranded DNA cassette (generated using overlap extension PCR) containing the 5'UTR (500 nt) of *CDC42* followed by the open reading frame with an SGGSHHHHHH-mCherry-SGGs insertion at Leucine 134, followed by the *HIS3* auxotrophic marker amplified from pFA6a-GFP-HISMx6, followed by 3'UTR (500 nt) of *CDC42*. His⁺Leu⁻ diploid transformants were then sporulated and dissected to obtain the *CDC42-mCherry^{SW}::HIS* haploid. Strains were propagated using standard techniques (Amberg). For *VPS21*

overexpression, the 500-nt promoter region of *ADHI* was integrated at *VPS21* through Longtine integration of a KanMX::ADHI_{Pr} cassette.

Plasmids

All plasmids used are listed in Table S3. pFA6a-GFP-HIS3MX6 (Longtine) was used for the PCR integration of C-terminal GFP fusions of endogenous genes. pFA6a-link-yomCherry-KanR (Lee et al., 2013) was used for the PCR integration of C-terminal mCherry fusions of endogenous genes. Gene deletion cassettes were PCR amplified from *cgLEU* or *cgURA* that was cloned into pBluescript vectors. The NLS-GFP plasmid PLPC18 was provided by Patrick Lusk (Webster Cell) and is a pRS406 plasmid containing the NLS sequence of *HEH2* followed by 3x GFP under the control of the *PHO4* promoter. The *GFP-HDEL::LEU* plasmid used was a gift from Laura Lackner (unpublished) and is a pRS305 plasmid containing the promoter of *TPII*, followed by the leader sequence of *KAR2* (aa 1–52), followed by GFP, followed by HDEL. The URA version of the plasmid was made by subcloning the *TPII-KAR2-GFP-HDEL* fragment into pRS306. For GST-fusion protein expression, Chm7, Heh2, and Snf7 fragments were cloned into pGEX-4T-1 (GE Lifesciences) vector using BamHI and XhoI. The following fragments were used: Heh2^{N-Terminal} is aa 1–308, Heh2^{C-Terminal} is aa 566–663, Snf7^{open} is aa 1–156, Snf7^{Full-length(FL)} is aa 1–240, Chm7^{open} is aa 1–369, and Chm7^{FL} is aa 1–450. For His₆-Cdc42^{Q61L} protein purification, full-length Cdc42 with a Q61L point mutation was cloned into a pBH-based vector (Smith and Prehoda, 2011) containing a Tobacco Etch Virus protease-cleavable N-terminal 6x-His epitope using BamHI and XhoI.

Fluorescence microscopy

Cells were grown to early- to mid-log phase (OD₆₀₀ 0.1–0.7 reading on Ultrospec 10 Cell Density Meter; Amersham) from an overnight 1:50 to 1:100 dilution of a log phase culture in imaging media (synthetic minimal media supplemented with adenine, l-histidine, l-leucine, l-lysine, l-methionine, uracil, and 2% glucose). Cells were adhered to 25-mm, 1.5-thickness circular coverslips (Deckgläser) coated with 0.2 mg/ml concanavalin A.

Epifluorescence imaging was performed on a Nikon Eclipse Ti inverted microscope with a Nikon 100× 1.4-NA Plan Apo VC oil-immersion objective and an Andor Neo 5.5 scientific complementary metal-oxide-semiconductor (sCMOS) camera. GFP and mCherry fluorescence were excited using a Lumencor Spectra X light-emitting diode light source with 470/22-nm and 575/25-nm excitation filters, respectively. For GFP-mCherry two-color imaging, channels were acquired sequentially using an FF-596-Di01-25 × 36 dual-pass dichroic mirror and FF01-641/75-25 dual-pass emission filters (Semrock). The system was controlled with Nikon Elements software and kept in a room maintained at 23°–25°C.

Spinning-disk confocal imaging was performed on the Eclipse Ti inverted microscope outfitted with a Nikon 100× 1.45-NA Plan Apo VC or Nikon 60× 1.4-NA Plan Apo VC oil-immersion objective lens, a Yokogawa CSU-X1 spinning disk, and Andor iXon^{EM} DU-897 electron multiplying charge coupled device (EMCCD) camera. GFP, mCherry, and mtagBFP2 fluorescence was excited using 488-nm, 561-nm, and 405-nm lasers,

respectively, and detected with Chroma 535/20-nm, Chroma 605/52-nm, and 470/40-nm emission filters, respectively. The system was controlled with Elements software and kept in a room maintained at 23°–25°C.

GST pulldown assays

Purified GST-Heh2^{NT} (860 nM), purified GST-Heh2^{CT} (900 nM), purified GST-Snf7^{FL} (200 nM), purified GST-Snf7^{open} (280 nM), 1,000 μl GST-Chm7^{FL} bacterial lysate, and 1,000 μl GST-Chm7^{open} were brought up to 1,000 μl in transport buffer (20 mM Hepes, pH 7.5, 110 mM KOAc, 2 mM MgCl₂, 1% Triton X-100, and 1 mM DTT) and incubated with 25 μl glutathione agarose (50:50 [vol/vol] slurry in deionized H₂O) at 4°C for 1 h. Beads were then washed in 500 μl cold transport buffer three times. Purified His₆-Cdc42 was then added to the beads at a concentration of 2.1 μM to a final reaction volume of 100 μl, then incubated at 4°C for 1 h with slight agitation. The beads were then washed in 500 μl transport buffer three times. Proteins were eluted with 13 μl 6x SDS sample buffer (125 mM Tris, pH 6.8, 30% glycerol [vol/vol], 4.1% SDS [wt/vol], and 20 mM DTT).

SDS-PAGE and Western blotting

13 μl of the GST pulldown assay eluates were resolved by SDS-PAGE and either stained with GelCode Blue Stain reagent (Thermo) or transferred onto 0.2-μm nitrocellulose (Amersham Protran) in 25 mM Tris, 120 mM glycine, and 20% methanol. Nitrocellulose membranes were then dried for 30 min and blocked in 5% milk in TBS for 30 min. Mouse anti-His primary antibody (R&D Systems) was used at 1:1,000 dilution in TBS, 1% Tween-20, and 1% block and applied for 1 h at room temperature. Blot was washed for 15 min in TBS + 1% Tween-20, and then IRDye 800CW goat anti-mouse secondary antibody (Li-Cor) was used at 1:10,000 dilution in TBS + 1% Tween-20, 0.1% block, and incubated at room temperature for 1 h. Blot was then washed for 30 min in TBS + 1% Tween-20 and imaged using an Odyssey CLx (Li-Cor).

Production of recombinant proteins

All proteins were expressed and purified from *Escherichia coli* Rosetta (DE3) Competent Cells (Novagen). Details of individual constructs and their expression plasmids are detailed in the Plasmids section. For GST-fusion proteins, cells were grown in LB + ampicillin (100 μg/ml) + chloramphenicol (25 μg/ml) to mid-log phase, and expression was induced with 250 μM IPTG for 16 h at 18°C. Cells were pelleted and resuspended in PBS + Complete Mini EDTA-free protease inhibitor (Roche). Cells were lysed by sonication using a W-385 Sonicator Ultrasonic Processor (Heat Systems; Ultrasonics, Inc), using 1 min of 0.5 s on/0.5 s off cycling for two cycles. Crude lysates were then adjusted to contain 1% Triton X-100 and clarified by spinning at 25,000 rpm in a Ti-70 rotor. Clarified lysates were applied to 1 mL glutathione agarose (Sigma), incubated at 4°C for an hour, washed with 150 ml PBS + 1% Triton X-100, and then eluted with 30 mM reduced glutathione in 50 mM Tris, pH 9.5. GST-fusion protein eluates were then dialyzed overnight at 4°C in 25 mM Tris, pH 7.5, 150 mM NaCl, and 1 mM DTT using a Slide-A-Lyzer 10-kD molecular weight cut-off dialysis cassette (Thermo). The

following day, dialysates were concentrated over a 10k, 30k, or 50k Amicon Ultra-4 Centrifugal filter (Millipore). Concentrated, purified protein was aliquoted, snap frozen in liquid nitrogen, and stored at -80°C .

For His₆-Cdc42^{Q61L} purification, protein expression was performed as described for GST-fusion proteins. Harvested cells were pelleted and resuspended in PBS + 20 mM imidazole. Cell lysis and lysate clarification were performed as described above. Clarified lysate was then incubated with 1 ml nickel nitrilotriacetic acid (Ni-NTA) agarose (Invitrogen) for 1 h at 4°C . Beads were then washed in 150 ml PBS + 20 mM imidazole, and protein was eluted with 250 mM imidazole. Eluate was then desalted over a PD-10 column (GE Lifesciences) into 50 mM Tris, pH 8.0, and 150 mM NaCl and polished over a mono Q 5/50 GL anion exchange column (GE Lifesciences). Bound proteins were eluted off over 20 column volumes to 35% elution buffer (50 mM Tris, pH 8.0, and 1 M NaCl). Eluates were dialyzed overnight against 25 mM Tris, pH 7.5, 150 mM NaCl, and 1 mM DTT using a Slide-A-Lyzer 10-kD MWCO dialysis cassette. The following morning, the purified protein was concentrated over a 10k Amicon Ultra-4 Centrifugal filter and then immediately aliquoted, snap frozen in liquid nitrogen, and stored at -80°C until further use.

The concentrations of purified proteins were measured by SDS-PAGE using GelCode Blue Stain Reagent to visualize protein bands. The quantification of Coomassie-stained bands was determined using an Odyssey CLx and its accompanying software. Ultra-pure bovine serum albumin supplied in the BCA Protein Assay kit (Thermo) was used to generate a standard curve.

Imaging processing and analysis

All micrographs were acquired using Nikon Elements imaging software. All images were processed using FIJI/ImageJ. Kymographs in Fig. 1, C and D; and Fig. 2, A–C were generated from maximum-intensity projections of $2\text{ }\mu\text{m}$ at $0.5\text{-}\mu\text{m}$ steps using a 1-pixel line drawn across the Cdc42 spot. The “Plot profile” tool was used to obtain intensity values as a function of distance, which were then exported and replotted in PRISM (GraphPad) as values normalized to the maximum value.

To measure the nuclear accumulation of NLS-GFP, we measured the GFP fluorescence intensity of a $0.5\text{-}\mu\text{m}^2$ area in the nucleus and a $0.5\text{-}\mu\text{m}^2$ area in the cytoplasm from maximum-intensity projection images of $11\text{ }\mu\text{m}$ at $0.5\text{-}\mu\text{m}$ steps. The background was averaged and subtracted from NLS-GFP values, and the nuclear accumulation was plotted as a mean ratio of nuclear and cytoplasmic measurements. Individual cell measurements are presented in Table S1.

Frequency distributions shown in Fig. 5, C and D were generated from measurements taken from 20 cells per trial for two trials using 16-bit grayscale images. A single focal plane at the thickest part of the cell was analyzed instead of intensity projections because of the large variation in cell size of the mutant strain. A boundary was drawn around the edge of the cell’s medial focal plane (cell cortex boundary determined by cortical GFP-HDEL in the green channel) using the “Freehand selections” tool in ImageJ; then a histogram of pixel intensities was generated using the “Histogram” function with the bin-width set to one. The area in micrometer squared of the cell was then

measured using the “Measure” function, and this value was used to normalize pixel counts to area. The frequency distribution values were then replotted using PRISM (GraphPad) software. The mean is represented by the thick line, and the standard deviation is represented as 1-pt vertical lines.

To determine the ER area/cell area ratio for each cell, ImageJ was used to analyze 16-bit confocal spinning-disk micrographs of a single focal plane at each cell’s thickest portion. The Freehand selection tool was used to outline the boundary of each cell. Then, the boundary pixels were thresholded using the “moment” algorithm (Tsai, 1985) and converted to binary. ER area was calculated as percentage of signal pixels (255 value pixels) to total pixels (sum of 0-value pixels and 255-value pixels).

To determine the maximum intensity of the Cdc42 spot, ImageJ was used to analyze 16-bit confocal spinning-disk micrographs of maximum-intensity projections of $7\text{ }\mu\text{m}$ at $0.5\text{-}\mu\text{m}$ steps. Both cells overexpressing VPS21 and wild-type cells (also expressing GFP-HDEL to distinguish from mutants) were imaged in the same field of view. The “Oval” tool was used to boundary the Cdc42 spot, and the maximum intensity was measured.

To determine the degree of colocalization of Vps4 and Snf7, ImageJ was used to analyze 16-bit confocal spinning-disk micrographs of a single focal plane at each cell’s thickest portion. Individual cells were cropped to ensure single-cell analysis, and the JACoP plug-in (Bolte and Cordelières, 2006) was used to obtain the Pearson’s correlation coefficient for each cell analyzed.

Equilibrium binding assay

Purified GST-Snf7^{open} was immobilized onto $12.5\text{ }\mu\text{l}$ glutathione agarose beads in a total volume of $100\text{ }\mu\text{l}$ to a final concentration of $11\text{ }\mu\text{M}$, $23\text{ }\mu\text{M}$, $7\text{ }\mu\text{M}$, $68\text{ }\mu\text{M}$, or $114\text{ }\mu\text{M}$ in transport buffer (20 mM Hepes, pH 7.5, 110 mM KOAc, 2 mM MgCl₂, 1% Triton X-100, and 1 mM DTT) and incubated for 1 h at 4°C . Beads were then washed twice in $500\text{ }\mu\text{l}$ transport buffer. Purified His₆-Cdc42 was then added to the beads in a total volume of $50\text{ }\mu\text{l}$ brought up with transport buffer to a final concentration of $0.44\text{ }\mu\text{M}$ and incubated for 1 h at 4°C . The supernatant was then recovered, and unbound Cdc42 was analyzed by SDS-PAGE followed by Western blotting. PRISM was used to plot % Cdc42 bound versus Snf7 concentration, and the nonlinear fit function was used to obtain the dissociation constant.

Online supplemental material

Fig. S1 shows growth assay of the Cdc42-mCherry^{SW} strain, as well as additional examples of the Cdc42 focus in the mother, bud, and mother and bud. It also shows a montage from Video 1 and contains a cartoon illustration of the ER and nuclear membrane architecture. Fig. S2 shows additional localization fluorescence microscopy micrographs of the Cdc42 spot at the vacuole and ER membranes and a montage taken from Video 4 of the Cdc42 spot at the vertices of fusing vacuoles. Fig. S3 shows additional experiments demonstrating that the leaky nucleus and ER phenotypes of *cdc42-129* mutant are not due to pleiotropy, that the leaky nucleus phenotype and SINC formation are not correlated, that Vps4 and Snf7 colocalization is not affected

in *cdc42-129* mutants, and the decreased binding affinity for Snf7 exhibited by the *Cdc42^{V36T}* mutant (product of *cdc42-129* allele). **Video 1** shows the *Cdc42* spot segregating to the bud during division. **Video 2** shows the *Cdc42* spot localizing to the base of an ER tubule undergoing fission. **Video 3** shows the *Cdc42* spot localizing to the base of the neck of the nuclear envelope undergoing fission. **Video 4** shows the *Cdc42* spot localizing to vertices of fusing vacuole fragments. **Video 5** shows the *Cdc42* and Snf7 colocalized spot migrating to the base of the neck of the nuclear envelope undergoing fission. **Video 6** shows that *Cdc42* and SINC (visualized by Nup188-GFP aggregate) do not migrate together during cell division. Table S1 shows the measurements made for every cell of every trial for quantifications shown in **Fig. 3 E**. Table S2 presents the strains used in this study. Table S3 presents the strains used in this study.

Acknowledgments

We thank Patrick Lusk and Laura Lackner for generously providing plasmids. We thank Ross Pedersen and James Hurley for critically evaluating the manuscript and members of the Drubin/Barnes laboratory for constant informal input. We thank H. Aaron for her microscopy training and assistance.

Spinning-disk confocal microscopy was conducted at the University of California, Berkeley, Cancer Research Laboratory Molecular Imaging center, supported by the Gordon and Betty Moore Foundation. This work was supported by the National Institutes of Health grant no. R35GM118149 to D.G. Drubin.

The authors declare no competing financial interests.

Author contributions: M.S. Lu and D.G. Drubin conceived of the experiments. M.S. Lu generated the reagents, performed the experiments, and analyzed the data. M.S. Lu and D.G. Drubin wrote the manuscript. D.G. Drubin secured funding.

Submitted: 17 October 2019

Revised: 11 March 2020

Accepted: 1 May 2020

References

- Adamo, J.E., J.J. Moskow, A.S. Gladfelter, D. Viterbo, D.J. Lew, and P.J. Brennwald. 2001. Yeast *Cdc42* functions at a late step in exocytosis, specifically during polarized growth of the emerging bud. *J. Cell Biol.* 155:581–592. <https://doi.org/10.1083/jcb.200106065>
- Adams, A.E., D.I. Johnson, R.M. Longnecker, B.F. Sloat, and J.R. Pringle. 1990. *CDC42* and *CDC43*, two additional genes involved in budding and the establishment of cell polarity in the yeast *Saccharomyces cerevisiae*. *J. Cell Biol.* 111:131–142. <https://doi.org/10.1083/jcb.111.1.131>
- Adell, M.A., G.F. Vogel, M. Pakdel, M. Müller, H. Lindner, M.W. Hess, and D. Teis. 2014. Coordinated binding of Vps4 to ESCRT-III drives membrane neck constriction during MVB vesicle formation. *J. Cell Biol.* 14:33–49. <https://doi.org/10.1083/jcb.201310114>
- Adell, M.A.Y., S.M. Migliano, S. Upadhyayula, Y.S. Bykov, S. Sprenger, M. Pakdel, G.F. Vogel, G. Jih, W. Skillern, R. Behrouzi, et al. 2017. Recruitment dynamics of ESCRT-III and Vps4 to endosomes and implications for reverse membrane budding. *eLife*. 6. e31652. <https://doi.org/10.7554/eLife.31652>
- Bendezú, F.O., V. Vincenzetti, D. Vavylonis, R. Wyss, H. Vogel, and S.G. Martin. 2015. Spontaneous *Cdc42* polarization independent of GDI-mediated extraction and actin-based trafficking. *PLoS Biol.* 13. e1002097. <https://doi.org/10.1371/journal.pbio.1002097>
- Bolte, S., and F.P. Cordelières. 2006. A guided tour into subcellular colocalization analysis in light microscopy. *J. Microsc.* 224:213–232. <https://doi.org/10.1111/j.1365-2818.2006.01706.x>
- Cashikar, A.G., S. Shim, R. Roth, M.R. Maldazys, J.E. Heuser, and P.I. Hanson. 2014. Structure of cellular ESCRT-III spirals and their relationship to HIV budding. *eLife*. 3. e02184. <https://doi.org/10.7554/eLife.02184>
- De Franceschi, N., M. Alqabandi, N. Miguët, C. Caillat, S. Mangelot, W. Weissenhorn, and P. Bassereau. 2019. The ESCRT protein CHMP2B acts as a diffusion barrier on reconstituted membrane necks. *J. Cell Sci.* 132. jcs217968. <https://doi.org/10.1242/jcs.217968>
- Du, Y., S. Ferro-Novick, and P. Novick. 2004. Dynamics and inheritance of the endoplasmic reticulum. *J. Cell Sci.* 117:2871–2878. <https://doi.org/10.1242/jcs.01286>
- Eitzen, G., N. Thorngren, and W. Wickner. 2001. Rho1p and *Cdc42p* act after Ypt7p to regulate vacuole docking. *EMBO J.* 20:5650–5656. <https://doi.org/10.1093/emboj/20.20.5650>
- Estrada, P., J. Kim, J. Coleman, L. Walker, B. Dunn, P. Takizawa, P. Novick, and S. Ferro-Novick. 2003. Myo4p and She3p are required for cortical ER inheritance in *Saccharomyces cerevisiae*. *J. Cell Biol.* 163:1255–1266. <https://doi.org/10.1083/jcb.200304030>
- Etienne-Manneville, S.. 2004. *Cdc42*—the centre of polarity. *J. Cell Sci.* 117: 1291–1300. <https://doi.org/10.1242/jcs.01115>
- Fehrenbacher, K.L., D. Davis, M. Wu, I. Boldogh, and L.A. Pon. 2002. Endoplasmic reticulum dynamics, inheritance, and cytoskeletal interactions in budding yeast. *Mol. Biol. Cell.* 13:854–865. <https://doi.org/10.1091/mbc.01-04-0184>
- Garrard, S.M., C.T. Capaldo, L. Gao, M.K. Rosen, I.G. Macara, and D.R. Tomchick. 2003. Structure of *Cdc42* in a complex with the GTPase-binding domain of the cell polarity protein, Par6. *EMBO J.* 22: 1125–1133. <https://doi.org/10.1093/emboj/cdg110>
- Gonzalez, Y., A. Saito, and S. Sazer. 2012. Fission yeast Lem2 and Man1 perform fundamental functions of the animal cell nuclear lamina. *Nucleus*. 3:60–76. <https://doi.org/10.4161/nucl.18824>
- Gotta, M., M.C. Abraham, and J. Ahringer. 2001. *CDC-42* controls early cell polarity and spindle orientation in *C. elegans*. *Curr. Biol.* 11:482–488. [https://doi.org/10.1016/S0960-9822\(01\)00142-7](https://doi.org/10.1016/S0960-9822(01)00142-7)
- Gu, M., D. LaJoie, O.S. Chen, A. von Appen, M.S. Ladinsky, M.J. Redd, L. Nikolova, P.J. Bjorkman, W.I. Sundquist, K.S. Ullman, et al. 2017. LEM2 recruits CHMP7 for ESCRT-mediated nuclear envelope closure in fission yeast and human cells. *Proc. Natl. Acad. Sci. USA*. 114:E2166–E2175. <https://doi.org/10.1073/pnas.1613916114>
- Guo, E.Z., and Z. Xu. 2015. Distinct mechanisms of recognizing endosomal sorting complex required for transport III (ESCRT-III) protein IST1 by different microtubule interacting and trafficking (MIT) domains. *J. Biol. Chem.* 290:8396–8408. <https://doi.org/10.1074/jbc.M114.607903>
- Hanson, P.I., R. Roth, Y. Lin, and J.E. Heuser. 2008. Plasma membrane deformation by circular arrays of ESCRT-III protein filaments. *J. Cell Biol.* 180:389–402. <https://doi.org/10.1083/jcb.200707031>
- Henne, W.M., N.J. Buchkovich, Y. Zhao, and S.D. Emr. 2012. The endosomal sorting complex ESCRT-II mediates the assembly and architecture of ESCRT-III helices. *Cell*. 151:356–371. <https://doi.org/10.1016/j.cell.2012.08.039>
- Kay, A.J., and C.P. Hunter. 2001. *CDC-42* regulates PAR protein localization and function to control cellular and embryonic polarity in *C. elegans*. *Curr. Biol.* 11:474–481. [https://doi.org/10.1016/S0960-9822\(01\)00141-5](https://doi.org/10.1016/S0960-9822(01)00141-5)
- Kieffer, C., J.J. Skalicky, E. Morita, I. De Domenico, D.M. Ward, J. Kaplan, and W.I. Sundquist. 2008. Two distinct modes of ESCRT-III recognition are required for VPS4 functions in lysosomal protein targeting and HIV-1 budding. *Dev. Cell*. 15:62–73. <https://doi.org/10.1016/j.devcel.2008.05.014>
- Kim, A.S., L.T. Kakalis, N. Abdul-Manan, G.A. Liu, and M.K. Rosen. 2000. Autoinhibition and activation mechanisms of the Wiskott-Aldrich syndrome protein. *Nature*. 404:151–158. <https://doi.org/10.1038/35004513>
- King, M.C., C.P. Lusk, and G. Blobel. 2006. Karyopherin-mediated import of integral inner nuclear membrane proteins. *Nature*. 442:1003–1007. <https://doi.org/10.1038/nature05075>
- Kozminski, K.G., A.J. Chen, A.A. Rodal, and D.G. Drubin. 2000. Functions and functional domains of the GTPase *Cdc42p*. *Mol. Biol. Cell*. 11:339–354. <https://doi.org/10.1091/mbc.11.1.339>
- Lee, S., W.A. Lim, and K.S. Thorn. 2013. Improved blue, green, and red fluorescent protein tagging vectors for *S. cerevisiae*. *PLoS One*. 8. e67902. <https://doi.org/10.1371/journal.pone.0067902>
- Lee, I.H., H. Kai, L.A. Carlson, J.T. Groves, and J.H. Hurley. 2015. Negative membrane curvature catalyzes nucleation of endosomal sorting

- complex required for transport (ESCRT)-III assembly. *Proc. Natl. Acad. Sci. USA*. 112:15892–15897. <https://doi.org/10.1073/pnas.1518765113>
- Lee, I.J., E. Stokasimov, N. Dempsey, J.M. Varberg, E. Jacob, S.L. Jaspersen, and D. Pellman. 2020. Factors promoting nuclear envelope assembly independent of the canonical ESCRT pathway. *J. Cell Biol.* 219. e201908232. <https://doi.org/10.1083/jcb.201908232>
- Longtine, M.S., A. McKenzie, III, D.J. Demarini, N.G. Shah, A. Wach, A. Brachat, P. Philippsen, and J.R. Pringle. 1998. Additional modules for versatile and economical PCR-based gene deletion and modification in *Saccharomyces cerevisiae*. *Yeast*. 14:953–961. [https://doi.org/10.1002/\(SICI\)1097-0061\(199807\)14:10<953::AID-YEA293>3.0.CO;2-U](https://doi.org/10.1002/(SICI)1097-0061(199807)14:10<953::AID-YEA293>3.0.CO;2-U)
- McCullough, J., M. Saunders, L. Colf, W. Sundquist, and A. Frost. 2015. Structure and Function of Membrane-Remodeling ESCRT-III Assemblies. *Biophys. J.* 108:358a. <https://doi.org/10.1016/j.bpj.2014.11.1960>
- Müller, O., D.I. Johnson, and A. Mayer. 2001. Cdc42p functions at the docking stage of yeast vacuole membrane fusion. *EMBO J.* 20:5657–5665. <https://doi.org/10.1093/emboj/20.20.5657>
- Obita, T., S. Saksena, S. Ghazi-Tabatabai, D.J. Gill, O. Perisic, S.D. Emr, and R.L. Williams. 2007. Structural basis for selective recognition of ESCRT-III by the AAA ATPase Vps4. *Nature*. 449:735–739. <https://doi.org/10.1038/nature06171>
- Olmos, Y., L. Hodgson, J. Mantell, P. Verkade, and J.G. Carlton. 2015. ESCRT-III controls nuclear envelope reformation. *Nature*. 522:236–239. <https://doi.org/10.1038/nature14503>
- Olmos, Y., A. Perdrix-Rosell, and J.G. Carlton. 2016. Membrane Binding by CHMP7 Coordinates ESCRT-III-Dependent Nuclear Envelope Reformation. *Curr. Biol.* 26:2635–2641. <https://doi.org/10.1016/j.cub.2016.07.039>
- Penfield, L., R. Shankar, E. Szentgyörgyi, A. Laffitte, M.S. Mauro, A. Audhya, T. Müller-Reichert, and S. Bahmanyar. 2020. Regulated lipid synthesis and LEM2/CHMP7 jointly control nuclear envelope closure. *J. Cell Biol.* 219. e201908179. <https://doi.org/10.1083/jcb.201908179>
- Prehoda, K.E., J.A. Scott, R.D. Mullins, and W.A. Lim. 2000. Integration of multiple signals through cooperative regulation of the N-WASP-Arp2/3 complex. *Science*. 290:801–806. <https://doi.org/10.1126/science.290.5492.801>
- Preuss, D., J. Mulholland, C.A. Kaiser, P. Orlean, C. Albright, M.D. Rose, P.W. Robbins, and D. Botstein. 1991. Structure of the yeast endoplasmic reticulum: localization of ER proteins using immunofluorescence and immunoelectron microscopy. *Yeast*. 7:891–911. <https://doi.org/10.1002/yea.320070902>
- Prinz, W.A., L. Grzyb, M. Veenhuis, J.A. Kahana, P.A. Silver, and T.A. Rapoport. 2000. Mutants affecting the structure of the cortical endoplasmic reticulum in *Saccharomyces cerevisiae*. *J. Cell Biol.* 150:461–474. <https://doi.org/10.1083/jcb.150.3.461>
- Saksena, S., J. Wahlman, D. Teis, A.E. Johnson, and S.D. Emr. 2009. Functional reconstitution of ESCRT-III assembly and disassembly. *Cell*. 136: 97–109. <https://doi.org/10.1016/j.cell.2008.11.013>
- Schöneberg, J., I.H. Lee, J.H. Iwasa, and J.H. Hurley. 2017. Reverse-topology membrane scission by the ESCRT proteins. *Nat. Rev. Mol. Cell Biol.* 18: 5–17. <https://doi.org/10.1038/nrm.2016.121>
- Shen, Q.T., A.L. Schuh, Y. Zheng, K. Quinney, L. Wang, M. Hanna, J.C. Mitchell, M.S. Otegui, P. Ahlquist, Q. Cui, et al. 2014. Structural analysis and modeling reveals new mechanisms governing ESCRT-III spiral filament assembly. *J. Cell Biol.* 206:763–777. <https://doi.org/10.1083/jcb.201403108>
- Smith, N.R., and K.E. Prehoda. 2011. Robust spindle alignment in *Drosophila* neuroblasts by ultrasensitive activation of pins. *Mol. Cell*. 43:540–549. <https://doi.org/10.1016/j.molcel.2011.06.030>
- Stuchell-Brereton, M.D., J.J. Skalicky, C. Kieffer, M.A. Karren, S. Ghaffarian, and W.I. Sundquist. 2007. ESCRT-III recognition by VPS4 ATPases. *Nature*. 449:740–744. <https://doi.org/10.1038/nature06172>
- Tang, S., W.M. Henne, P.P. Borbat, N.J. Buchkovich, J.H. Freed, Y. Mao, J.C. Fromme, and S.D. Emr. 2015. Structural basis for activation, assembly and membrane binding of ESCRT-III Snf7 filaments. *eLife*. 4. e12548. <https://doi.org/10.7554/eLife.12548>
- Thaller, D.J., M. Allegretti, S. Borah, P. Ronchi, M. Beck, and C.P. Lusk. 2019. An ESCRT-LEM protein surveillance system is poised to directly monitor the nuclear envelope and nuclear transport system. *eLife*. 8. e45284. <https://doi.org/10.7554/eLife.45284>
- Tsai, W.-H. 1985. Moment-preserving thresholding: A new approach. *Comput. Vis. Graph. Image Process.* 29:377–393. [https://doi.org/10.1016/0734-189X\(85\)90133-1](https://doi.org/10.1016/0734-189X(85)90133-1)
- Vietri, M., K.O. Schink, C. Campsteijn, C.S. Wegner, S.W. Schultz, L. Christ, S.B. Thoresen, A. Brech, C. Raiborg, and H. Stenmark. 2015. Spastin and ESCRT-III coordinate mitotic spindle disassembly and nuclear envelope sealing. *Nature*. 522:231–235. <https://doi.org/10.1038/nature14408>
- Webster, B.M., P. Colombi, J. Jäger, and C.P. Lusk. 2014. Surveillance of nuclear pore complex assembly by ESCRT-III/Vps4. *Cell*. 159:388–401. <https://doi.org/10.1016/j.cell.2014.09.012>
- Webster, B.M., D.J. Thaller, J. Jäger, S.E. Ochmann, S. Borah, and C.P. Lusk. 2016. Chm7 and Hehl collaborate to link nuclear pore complex quality control with nuclear envelope sealing. *EMBO J.* 35:2447–2467. <https://doi.org/10.15252/emboj.201694574>
- Wiederkehr, A., Y. Du, M. Pypaert, S. Ferro-Novick, and P. Novick. 2003. Sec3p is needed for the spatial regulation of secretion and for the inheritance of the cortical endoplasmic reticulum. *Mol. Biol. Cell*. 14: 4770–4782. <https://doi.org/10.1091/mbc.e03-04-0229>
- Wu, C.F., J.G. Chiou, M. Minakova, B. Woods, D. Tsygankov, T.R. Zyla, N.S. Savage, T.C. Elston, and D.J. Lew. 2015. Role of competition between polarity sites in establishing a unique front. *eLife*. 4. e11611. <https://doi.org/10.7554/eLife.11611>
- Zhang, X., E. Bi, P. Novick, L. Du, K.G. Kozminski, J.H. Lipschutz, and W. Guo. 2001. Cdc42 interacts with the exocyst and regulates polarized secretion. *J. Biol. Chem.* 276:46745–46750.
- Zhu, L., J.R. Jorgensen, M. Li, Y.S. Chuang, and S.D. Emr. 2017. ESCRTs function directly on the lysosome membrane to downregulate ubiquitinated lysosomal membrane proteins. *eLife*. 6. e26403. <https://doi.org/10.7554/eLife.26403>

Supplemental material

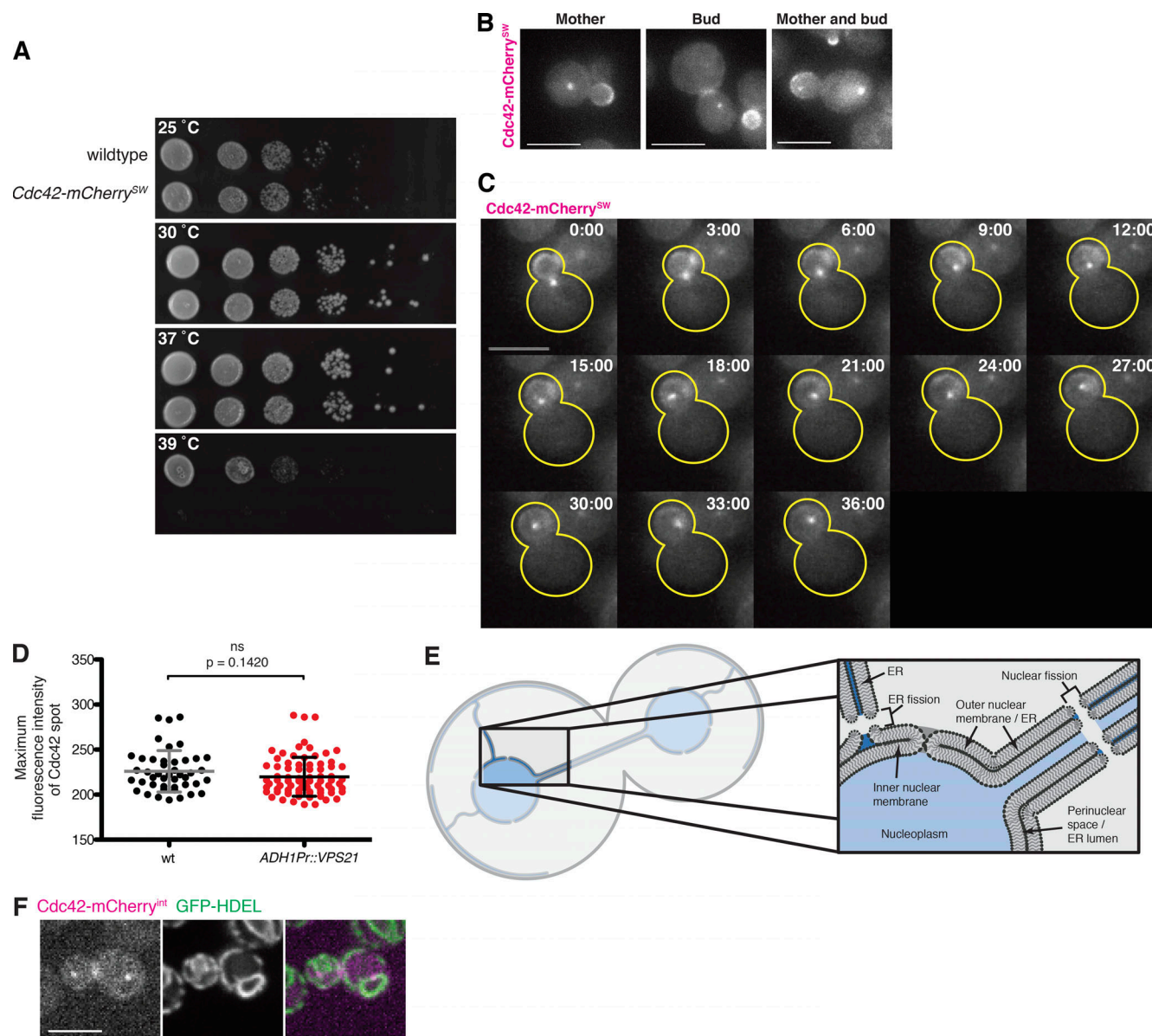


Figure S1. A functional internal fluorescent protein fusion of Cdc42 reveals a novel subcellular localization. (A) Cell growth of indicated yeast strains was compared by spotting serial dilutions of liquid cultures on plates at 25°C, 30°C, 37°C, or 39°C. (B) Micrographs of three separate cells expressing endogenous *Cdc42-mCherry^{SW}* showing *Cdc42* spot in the mother, the bud, or the mother and bud. (C) Montage of confocal spinning-disk movie stills of cells endogenously expressing *Cdc42-mCherry^{SW}* showing *Cdc42* spot segregating from mother cell into bud. Time is in minutes. (D) Quantification of maximum intensity of *Cdc42* spot in wild-type (wt) cells (black) or cells overexpressing *VPS21* (red) imaged at the restrictive temperature (37°C). Two trials each, mean \pm SD. wt: 226 ± 3.5 , $n = 44$. *VPS21* overexpression: 220 ± 2.4 , $n = 78$. No significant difference (ns; $P = 0.1420$) using Student's *t* test. (E) Illustration depicting the organization of membranes and lumen spaces of the nuclear envelope and ER. The perinuclear space is continuous with the ER lumen (dark blue) because the outer nuclear membrane is continuous with the ER membrane. Nuclear fission events introduce a break in the neck of the dividing nucleus to expose the nucleoplasm (light blue) to the cytosolic space. (F) Still images from epifluorescence movies of cells endogenously expressing *Cdc42-mCherry^{SW}* (magenta) and GFP-HDEL (green) to mark the ER and show the *Cdc42* spot on nuclear envelope after nuclear fission in both mother cells and buds. All cells in micrographs of this figure were imaged during log phase in minimal imaging media at 23°C–25°C. 2- μ m maximum-intensity projections at 0.5- μ m steps. All scale bars, 5 μ m.

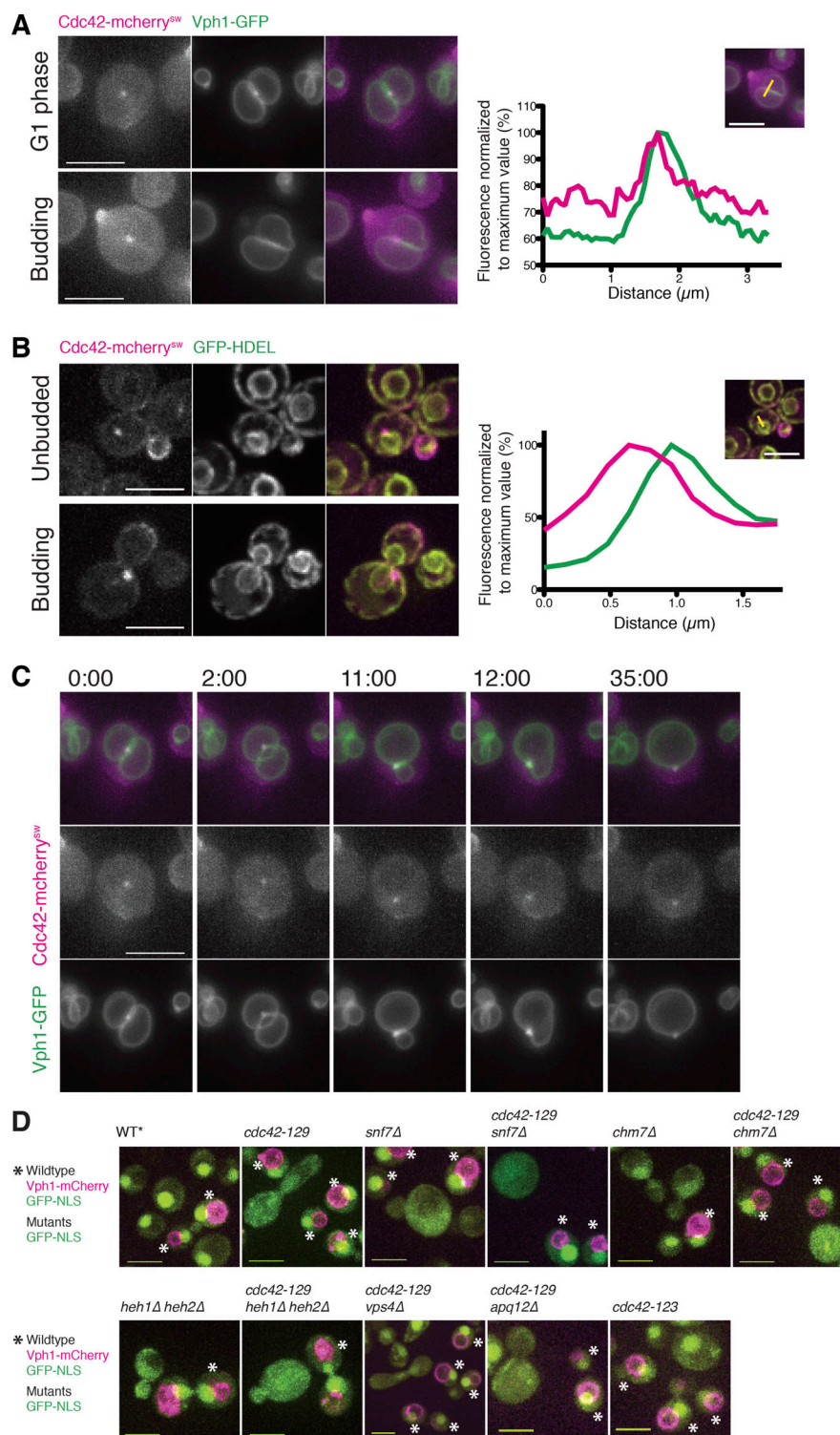


Figure S2. The Cdc42 spot is localized to vacuolar and ER membranes and vertices of fusing vacuoles. (A) Epifluorescence still images of cells endogenously expressing Cdc42-mCherry^{SW} (magenta) and Vph1-GFP (green) in unbudded (top panel) or budded cell (lower panel). Plot of normalized fluorescence intensity profiles of Vph1-GFP (green) and Cdc42-mCherry^{SW} (magenta) along yellow line shown in inset image. (B) Epifluorescence still images of cells endogenously expressing Cdc42-mCherry^{SW} (magenta) and GFP-HDEL (green) in unbudded (top panel) or budded cell (lower panel). Plot of normalized fluorescence intensity profiles of GFP-HDEL (green) and Cdc42-mCherry^{SW} (magenta) along yellow line shown in inset image. All images are 2- μm maximum-intensity projections at 0.5- μm steps. All scale bars, 5 μm . (C) Montage of stills from epifluorescence movies of cells expressing endogenous Cdc42-mCherry^{SW} (magenta) and Vph1-GFP (green). All cells in micrographs of this figure were imaged in log phase growth in minimal imaging media at 23°–25°C. Scale bar, 5 μm . 2- μm maximum-intensity projections at 0.5- μm steps. (D) Two-color versions of the micrographs in Fig. 3 D showing wild-type cells expressing Vph1-mCherry (marked with white asterisks in micrographs) in the same field of view as the mutant indicated by genotype above. Mutant and wild-type cells both express NLS-GFP. All scale bars, 5 μm .

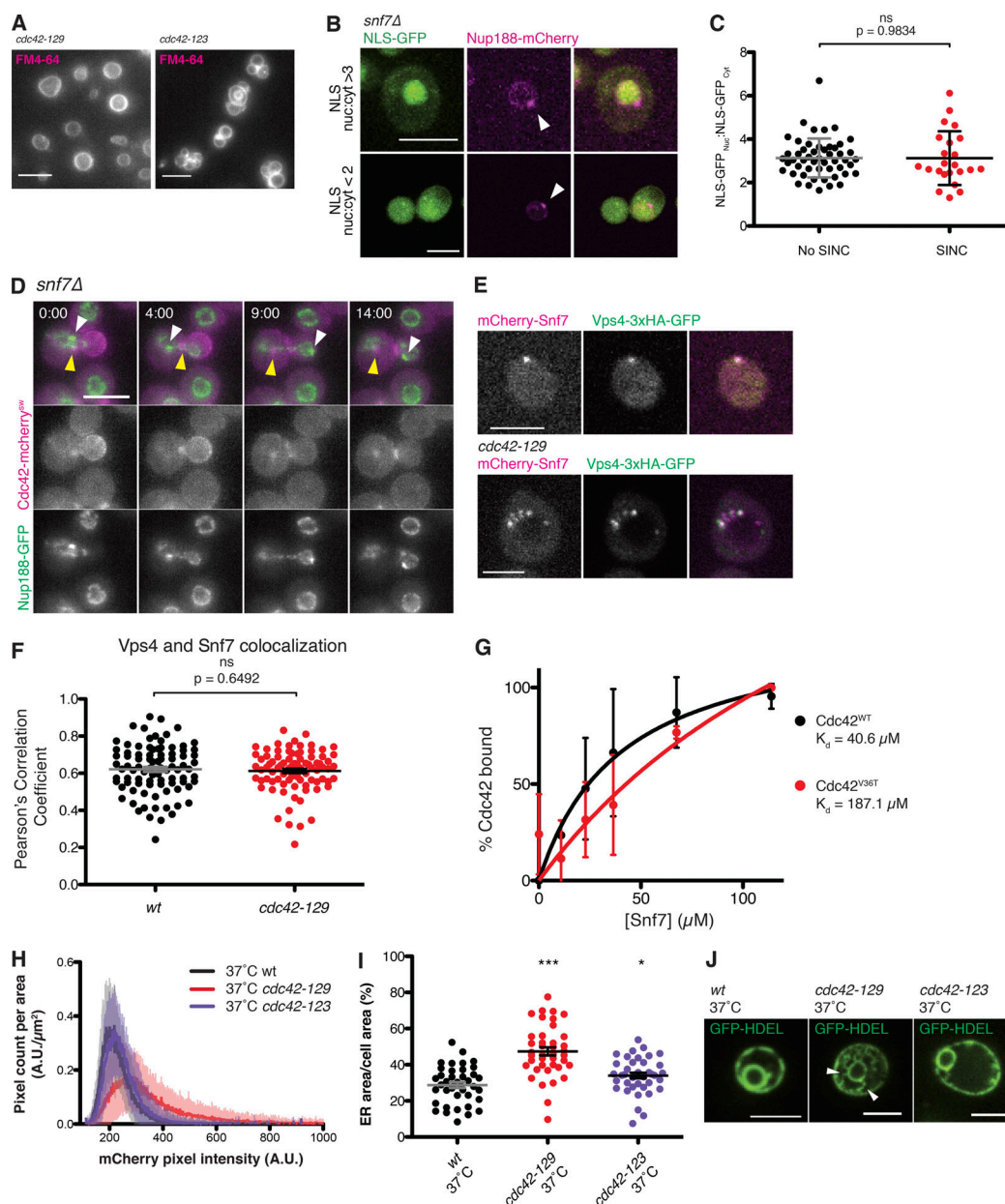


Figure S3. Leaky nucleus and ER phenotypes of *cdc42-129* mutant are not due to pleiotropy. (A) Still images from epifluorescence movies of *cdc42-129* (left) or *cdc42-123* (right) cells stained with FM4-64 to visualize the vacuole. 30-min pulse with FM4-64 (10 μ M) and chased 1 h. 2- μ m maximum-intensity projections at 0.5- μ m steps. (B) Confocal spinning-disk images of *snf7Δ* cells endogenously expressing NLS-GFP (green) and Nup188-mCherry (magenta). White arrowheads indicate SINC. Top panel is a cell with intact nucleo-cytoplasmic partitioning (NLS-GFP nucleus/cytoplasm ratio >3), and bottom panel is a cell with a leaky nucleus (NLS-GFP nucleus/cytoplasm ratio <3). 11- μ m maximum-intensity projection at 0.5- μ m steps. (C) Quantification of NLS-GFP nucleus/cytoplasm ratios of *snf7Δ* cells without (black) or with (red) a SINC. Two trials each, mean \pm SD. No SINC: 3.13 ± 0.13 , $n = 51$. SINC: 3.13 ± 0.26 , $n = 23$. No significant difference (ns; $P = 0.9834$) using Student's t test. nuc, nucleus; cyt, cytoplasm. (D) Montage of still images from epifluorescence movies of *snf7Δ* cells endogenously expressing Cdc42-mCherry^{int} (magenta) and Nup188-GFP (green). White arrowheads indicate SINC, and yellow arrowheads indicate Cdc42 spot. 2- μ m maximum-intensity projections at 0.5- μ m steps. (E) Epifluorescence stills of wild-type (top panel) or *cdc42-129* mutant cells (bottom panel) endogenously expressing mCherry-Snf7 (magenta) and Vps4-3xHA-GFP (green). 2- μ m maximum-intensity projections at 0.5- μ m steps. (F) Quantification of Vps4 and Snf7 colocalization in wild-type (wt; black) or *cdc42-129* (red) cells. Pearson's correlation coefficient. Two trials each, mean \pm SD. wt: 0.62 ± 0.01 , $n = 89$. *cdc42-129*: 0.61 ± 0.01 , $n = 84$. No significant difference ($P = 0.6429$) using Student's t test. (G) Plot of Snf7 equilibrium binding assay for Cdc42^{WT} (black) and Cdc42^{V36T} (red). Cdc42^{WT} K_d for Snf7 = 40.6 μ M; Cdc42^{V36T} K_d for Snf7 = 187.1 μ M. K_d = dissociation constant. Three independent trials were conducted for each experiment. Error bars represent standard deviation for three independent measurements. (H) Same quantification shown in Fig. 4 H, but with frequency distribution of Snf7 fluorescence intensity of *cdc42-123* mutants at 37°C overlaid in purple. Two trials, $n = 40$. A.U., arbitrary units. (I) Same quantification of ER area shown in Fig. 4 F for 37°C but with *cdc42-123* mutant measurements shown in purple circles. Two trials, $n = 40$, mean \pm SD. Asterisks denote statistical significance compared with control using Student's t test. *, $P \leq 0.05$; ***, $P \leq 0.001$. (J) Same micrographs shown in Fig. 4 E, but with *cdc42-123* micrograph included. Confocal spinning-disk micrographs of wild-type (left), *cdc42-129* (middle), and *cdc42-123* (right) cells expressing GFP-HDEL (green) to mark ER grown to early-log phase in minimal media and shifted to 37°C for 6 h. White arrowheads indicate ER tubules emanating from nuclear ER. Single (medial) focal plane. All cells in this figure were grown to log phase in minimal imaging media at 23°–25°C unless otherwise indicated. All scale bars, 5 μ m.

Video 1. **Cdc42 (magenta) spot segregates to bud during division. ER (green) shown to clarify cell boundary.** Scale bar, 5 μm . Time in minutes. 8 frames per second.

Video 2. **Cdc42 (magenta) spot localizes to the base of the neck of the nuclear envelope (green) undergoing fission.** Scale bar, 5 μm . Time in minutes. 8 frames per second.

Video 3. **Cdc42 (magenta) spot localizes to the base of an ER (green) tubule undergoing fission.** Scale bar, 5 μm . Time in minutes. 8 frames per second.

Video 4. **Cdc42 (magenta) spot localizes to vertices of fusing vacuole (green) fragments.** Scale bar, 5 μm . Time in minutes. 8 frames per second.

Video 5. **Cdc42 (red) and Snf7 (blue) colocalized spot migrate to the base of the neck of the nuclear envelope (green) undergoing fission.** Scale bar, 5 μm . Time in minutes. 8 frames per second.

Video 6. **Cdc42 (magenta) and SINC (visualized by Nup188-GFP [green] aggregate and indicated with arrow) do not migrate together during cell division.** Scale bar, 5 μm . Time in minutes. 10 frames per second.

Provided online are three tables. Table S1 is an Excel table that presents the measurements made for every cell of every trial for quantifications shown in Fig. 3 E. Table S2 presents the strains used in this study. Table S3 presents the plasmids used in this study.